Fundamenta Informaticae 41 (2000) 91–129
IOS Press

Curve Evolution, Differential Morphology, and Distance Transforms Applied to Multiscale and Eikonal Problems*

Petros Maragos†
Department of Electrical and Computer Engineering
National Technical University of Athens
Zografou 15773, Athens, Greece.
maragos@cs.ntua.gr

Muhammad Akmal Butt
Communications Enabling Technologies
Irvine, CA 92618, USA.
akmal@enabtech.com

Abstract. In differential morphology, multiscale dilations and erosions are modeled via nonlinear partial differential equations (PDEs) in scale-space. Curve evolution employs methods of differential geometry to study the differential equations governing the propagation of time-evolving curves, under velocities dependent on global information or on local geometric properties of the curve. The PDEs governing multiscale morphology, and most cases of curve evolution, are of the Hamilton-Jacobi type and are related to the eikonal PDE of optics. In this paper, we explore the common theoretical concepts, tools, and numerical algorithms used in differential morphology and curve evolution, by emphasizing level set methods. Morphological operator representations of various curve evolution cases are discussed, as well as evolution laws for various morphological curve operations. We also focus on distance transforms, as the major route to connect differential morphology and curve evolution to the eikonal PDE. Furthermore, we discuss applications of differential morphology and curve evolution to various multiscale and/or eikonal problems, such as distance transform computation, ray tracing in optics, eikonal image halftoning, and watershed-based image segmentation.

Keywords: computer vision, curve evolution, differential morphology, distance transforms, image processing.

*This work was done mainly when both authors were at Georgia Tech, Atlanta, USA, and was supported by the U.S. National Science Foundation, under Grant MIP-94-21677, and by the JSEP, under Grant DAAH-04-96-1-0161. The paper was written while P. Maragos was at the Institute for Language and Speech Processing, Athens, Greece.

†Address for correspondence: Department of Electrical and Computer Engineering, National Technical University of Athens, Zografou 15773, Athens, Greece.

1. Introduction

Detecting features, motion and objects, as well as modeling many other information extraction tasks in image processing and computer vision, has necessitated the analysis of image signals at multiple scales. Following the initial formulation and motivation of multiscale image analysis using Gaussian convolutions, by Marr and his co-workers [54], two other important developments were the continuous Gaussian scale-space by Witkin [90] and the observation by Koenderink [40] that this scale-space can be modeled via the heat diffusion *partial differential equation* (PDE). Specifically, if

$$u(x,y,t) = \iint_{\mathbb{R}^2} f(x-v, y-w) G_t(v,w) dv dw$$

is the multiscale linear convolution of an original image signal $f(x,y)$ with a Gaussian function

$$G_t(x,y) \triangleq \frac{1}{4\pi t} \exp(-\frac{x^2+y^2}{4t})$$

whose variance $(2t)$ is proportional to scale t, then the scale-space function u can be generated from the isotropic and homogeneous heat diffusion PDE[1]

$$\frac{\partial u}{\partial t} = \nabla^2 u = u_{xx} + u_{yy} \tag{1}$$

with initial condition $u(x,y,0) = f(x,y)$.

The popularity of this approach is due to its linearity and its relationship to the heat diffusion PDE, for which much is known from physics and mathematics. The big disadvantage of the Gaussian scale-space approach is the fact that linear smoothers blur and shift important image features, e.g., edges. There is, however, a variety of *nonlinear* smoothing filters, including morphological openings and closings [21, 47, 55, 76], open/closings by reconstruction [72], and anisotropic and nonlinear diffusion schemes [4, 63], that can smooth while preserving important image features and can provide a multiscale image ensemble, i.e., a nonlinear scale-space. Image smoothing, based on anisotropic and nonlinear diffusion, grew as an effort to improve Gaussian scale-space by smoothing away from, or parallel to, image edges. The morphological smoothing filters were developed independently from the Gaussian scale-space ideas and correspond to simple min-max filtering operations.

Until recently, the vast majority of implementations of multiscale morphological filtering had been discrete. In 1992, inspired by the previous modeling of multiscale linear Gaussian convolutions of an image via the linear heat diffusion PDE, three teams of researchers independently published nonlinear PDEs that model the continuous multiscale morphological scale-space. Specifically, Alvarez, Guichard, Lions and Morel [2] obtained PDEs for multiscale flat dilation and erosion, by compact convex structuring sets, as part of their general work on developing PDE-based models for multiscale image processing that satisfy certain axiomatic principles.

[1] Notation often used for PDEs: $u_t = \partial u/\partial t$, $u_x = \partial u/\partial x$, $u_y = \partial u/\partial y$, $\nabla u = (u_x, u_y)$, $\mathrm{div}((v,w)) = \nabla \cdot (v,w) = v_x + w_y$.

Brockett and Maragos [16] developed PDEs that model multiscale morphological dilation, erosion, opening and closing by compact-support structuring elements that are either convex sets or concave functions and may have non-smooth boundaries or graphs, respectively. Their work was based on the semigroup structure of the multiscale dilation and erosion operators and the use of morphological sup/inf derivatives to deal with the development of shocks (i.e., discontinuities in the derivatives). In [83, Ch. 8], Boomgaard and Smeulders obtained PDEs for multiscale dilation and erosion by studying the propagation of the boundaries of 2D sets and the graphs of signals under multiscale dilation and erosion. Their work applies to convex structuring elements whose boundaries contain no linear segments, are smooth and possess a unique normal at each point. Refinements of the above three works for PDEs modeling multiscale morphology followed in [3, 5, 17, 34, 49, 84].

In parallel to the development of the above ideas, there have been some advances in the field of differential geometry for evolving curves or surfaces using level set methods. Specifically, Osher and Sethian [62, 78] have developed PDEs of the Hamilton-Jacobi type to model the propagation of curves, embedded as level curves (isoheight contours), of functions evolving in scale-space. The propagation was modeled using speeds along directions normal to the curve that contain a constant term and/or a term dependent on curvature. Furthermore, they developed robust numerical algorithms to solve these PDEs by using stable and shock-capturing schemes to solve similar, shock-producing, nonlinear wave PDEs that are related to hyperbolic conservation laws [41]. Kimia, Zucker and Tannenbaum [37] have applied and extended these curve evolution ideas to shape analysis in computer vision. Arehart, Vincent and Kimia [6] and Sapiro, Kimmel, Shaked, Kimia and Bruckstein [73] implemented continuous-scale morphological dilations and erosions using the numerical algorithms of curve evolution to solve the PDEs for multiscale dilation and erosion. There are several relationships between curve evolution and multiscale morphology, since the evolution with constant normal speed models multiscale set dilation, and the corresponding Hamilton-Jacobi PDEs contain the PDE of multiscale dilation/erosion by disks as a basic ingredient. Furthermore, the level sets used in curve evolution have previously been used extensively in mathematical morphology for extending set operations to functions.

A different viewpoint of multiscale morphological filtering is that, multiscale dilations and erosions of binary images can be obtained via distance transforms, i.e., the distance function from the original image set or its complement. Using Huygen's construction [15], the boundaries of multiscale dilations/erosions by disks can also be viewed as the wavefronts of a wave initiating from the original image boundary and propagating with constant normal speed, i.e., in a homogeneous medium. Thus, the distance function has a minimum time-of-arrival interpretation [13], and its isolevel contours coincide with those of the wave phase function. This idea can also be extended to wave propagation in heterogeneous media by using a weighted distance function, where the weights are inversely proportional to the propagation speeds [42]. In geometrical optics, which is the approximation of wave optics for very small wavelengths, the wavefronts are obtained from the isolevel contours of the eikonal function, which is proportional to the wave phase and satisfies the eikonal PDE. This ubiquitous PDE has been applied to solving

various problems in image analysis and computer vision, such as shape-from-shading, gridless halftoning, and image segmentation [35, 49, 50, 58, 61, 64, 69, 75, 85].

The previous discussion implies that the solution of the eikonal PDE is a weighted distance function. This solution is numerically approximated using discrete weighted distance transforms, which can be implemented either with 2D recursive min-sum difference equations [49, 70, 85] or with numerical algorithms of curve evolution [39]. The former implementation employs adaptive 2D recursive erosions and is a stationary approach for solving the eikonal equation, whereas the latter involves a time-dependent formulation and evolves curves based on a dilation-type PDE with speed varying according to the gray values.

This unified area of multiscale morphological PDEs and of the min-sum difference equations (which are recursive erosions), used to solve the eikonal equation, was called in [49] *differential morphology*. Whereas classical morphological image processing is based on set and lattice theory, differential morphology offers calculus-based tools and some exciting connections to the physics of wave propagation.

In this paper, we explore the theoretical and algorithmic relationships between differential morphology and curve evolution by emphasizing level set methods. Brief overviews of nonlinear PDEs modeling morphological scale-space and of curve evolution are also provided. Furthermore, morphological operator representations of various curve evolution cases are discussed, as well as evolution laws for various morphological curve operations. We also focus on distance transforms as the major route to connect differential morphology and curve evolution to the eikonal PDE. Finally, throughout the paper, we discuss applications of differential morphology and curve evolution to multiscale problems, such as distance transform computation, as well as to eikonal problems, such as ray tracing in optics, eikonal image halftoning, and image segmentation based on the watershed. Wherever possible, we compare the continuous PDE approach with the discrete approach.

2. PDEs Generating Multiscale Morphological Operations

The main tools of morphological image processing are a broad class of nonlinear signal operators formed as parallel and/or serial interconnections of the two most elementary morphological signal operators, the *dilation* $\oplus$ and the *erosion* $\ominus$:

$$(f \oplus g)(x) \stackrel{\triangle}{=} \bigvee_{y \in \mathbb{E}} f(y) + g(x-y)$$
$$(f \ominus g)(x) \stackrel{\triangle}{=} \bigwedge_{y \in \mathbb{E}} f(y) - g(y-x),$$

where $\bigvee$ and $\bigwedge$ denote supremum and infimum, and the signal domain can be continuous $\mathbb{E} = \mathbb{R}^d$ or discrete $\mathbb{E} = \mathbb{Z}^d$. The signal range is a subset of $\overline{\mathbb{R}} = \mathbb{R} \cup \{-\infty, +\infty\}$. The scalar addition in $\overline{\mathbb{R}}$ is like addition in $\mathbb{R}$ extended by the rules $a \pm \infty = \pm\infty$, $\forall a \in \mathbb{R}$, and $(+\infty) + (-\infty) = -\infty$. Compositions of erosions and dilations yield two useful smoothing filters: the *opening*

$f \mapsto (f \ominus g) \oplus g$ and *closing* $f \mapsto (f \oplus g) \ominus g$. The above morphological signal operations, and their combinations, have found a broad range of applications in image processing and computer vision; examples include problems in nonlinear filtering, noise suppression, contrast enhancement, geometric feature detection, skeletonization, multiscale analysis, size distributions, segmentation and shape recognition; see [33, 53, 76] for broad surveys and more references. In convex analysis [66] and optimization [10], the nonlinear operation $\oplus$ is called *supremal convolution* and an operation closely related to $\ominus$ is the *infimal convolution*

$$(f \oplus' g)(x) \stackrel{\triangle}{=} \bigwedge_{y \in \mathbb{E}} f(y) +' g(x-y)$$

where $+'$ is like the extended addition in $\overline{\mathbb{R}}$, except that $(+\infty) +' (-\infty) = +\infty$. Note that $\oplus'$ is closely related to $\ominus$ because $f \oplus' g = f \ominus (-g^r)$, where $g^r(x) = g(-x)$.

Let $K : \mathbb{R}^2 \to \overline{\mathbb{R}}$ be a unit-scale, upper-semicontinuous, concave structuring function. Scaling both its values and its support by a scale parameter $t \geq 0$ yields a parameterized family of multiscale structuring functions

$$K_t(x,y) \stackrel{\triangle}{=} \begin{cases} tK(x/t, y/t), & \text{if} \quad t > 0 \\ 0 \text{ at } (x,y) = (0,0) \text{ and } -\infty \text{ elsewhere}, & \text{if} \quad t = 0 \end{cases}$$

which satisfies the semigroup property

$$K_s \oplus K_t = K_{s+t}, \quad s, t \geq 0$$

Using K_t as the kernel in the basic morphological operations leads to defining the *multiscale dilation* and *erosion* of $f : \mathbb{R}^2 \to \mathbb{R}$ by K_t, as the scale-space functions

$$\begin{aligned} \delta(x,y,t) &\stackrel{\triangle}{=} (f \oplus K_t)(x,y) \\ \varepsilon(x,y,t) &\stackrel{\triangle}{=} (f \ominus K_t)(x,y), \end{aligned}$$

where $\delta(x,y,0) = \varepsilon(x,y,0) = f(x,y)$.

In practice, a useful class of functions K consists of *flat* structuring functions

$$K(x,y) = \begin{cases} 0, & (x,y) \in B \\ -\infty, & (x,y) \notin B \end{cases}$$

which are the supports of compact convex planar sets B. For flat K, the general multiscale dilations and erosions of f by K reduce to computing local suprema and infima of f within the scaled moving window $tB = \{(tx, ty) : (x,y) \in B\}$:

$$\begin{aligned} (f \oplus tB)(x,y) &\stackrel{\triangle}{=} \bigvee_{(a,b) \in tB} f(x-a, y-b) \\ (f \ominus tB)(x,y) &\stackrel{\triangle}{=} \bigwedge_{(a,b) \in tB} f(x+a, y+b). \end{aligned}$$

The general PDE generating the multiscale flat dilations of f by a general compact convex symmetric $B \subseteq \mathbb{R}^2$ is [2, 3, 16, 17, 56]

$$\frac{\partial \delta}{\partial t} = \mathrm{sptf}(B)\Big(\frac{\partial \delta}{\partial x}, \frac{\partial \delta}{\partial y}\Big) \tag{2}$$

where $\mathrm{sptf}(B)$ is the *support function* of B:

$$\mathrm{sptf}(B)(x,y) \stackrel{\triangle}{=} \bigvee_{(a,b)\in B} ax + by \tag{3}$$

Useful cases of structuring sets B are obtained by the unit balls

$$B_p = \{(x,y) \in \mathbb{R}^2 : ||(x,y)||_p \leq 1\}$$

of the metrics induced by the $||\cdot||_p$ norms:

$$||(x,y)||_p \stackrel{\triangle}{=} \begin{cases} (|x|^p + |y|^p)^{1/p}, & p = 1, 2, \ldots \\ \max(|x|, |y|), & p = \infty \end{cases}$$

The PDEs generating the multiscale flat dilations of f by B_p for three special cases of norms $||\cdot||_p$ are as follows [17]:

$$B = \text{rhombus } (p=1) \implies \delta_t = \max(|\delta_x|, |\delta_y|) = ||\nabla \delta||_\infty \tag{4}$$

$$B = \text{disk } (p=2) \implies \delta_t = \sqrt{(\delta_x)^2 + (\delta_y)^2} = ||\nabla \delta||_2 \tag{5}$$

$$B = \text{square } (p=\infty) \implies \delta_t = |\delta_x| + |\delta_y| = ||\nabla \delta||_1 \tag{6}$$

with $\delta(x,y,0) = f(x,y)$. The corresponding PDEs generating multiscale flat erosions are:

$$B = \text{rhombus} \implies \varepsilon_t = -||\nabla \varepsilon||_\infty$$

$$B = \text{disk} \implies \varepsilon_t = -||\nabla \varepsilon||_2$$

$$B = \text{square} \implies \varepsilon_t = -||\nabla \varepsilon||_1$$

with $\varepsilon(x,y,0) = f(x,y)$.

These simple, but nonlinear, PDEs are satisfied at points where the data are smooth, i.e., the partial derivatives exist. However, even if the initial image/signal f is smooth, at finite scales $t > 0$, the above dilation or erosion evolution may create discontinuities in the derivatives, called *shocks*, which then continue propagating in scale-space. Thus, the multiscale dilations δ, or erosions ε, are *weak solutions* of the corresponding PDEs in the sense of [41]. Ways to deal with these shocks include replacing standard derivatives with morphological derivatives [17, 49], or replacing the PDEs with differential inclusions [56]. For example, let

$$(\mathcal{M}_x f)(x,y) \stackrel{\triangle}{=} \lim_{r \downarrow 0} \frac{\sup\{f(x+v, y) : |v| \leq r\} - f(x,y)}{r}$$

be the sup-derivative of f along the x-direction. If the right $[f_x(x+,y)]$ and left $[f_x(x-,y)]$ derivatives of f along the x-direction exist, then [17]

$$(\mathcal{M}_x f)(x,y) = \max[0, f_x(x+,y), -f_x(x-,y)]$$

A similar statement can be made for the sup-derivative $\mathcal{M}_y f$ of f along the y-direction. Then, a generalized PDE generating flat dilations by a compact convex symmetric B is:

$$\frac{\partial \delta}{\partial t} = \mathrm{sptf}(B)(\mathcal{M}_x \delta, \mathcal{M}_y \delta)$$

This new PDE can handle discontinuities (i.e., shocks) in the partial derivatives of δ, provided that its left and right derivatives exist everywhere.

The above PDEs, for dilations/erosions of graylevel images by flat structuring elements, directly apply to binary images, because flat dilations/erosions commute with thresholding. Hence, when the graylevel image is dilated/eroded, each one of its thresholded versions, representing a binary image, is simultaneously dilated/eroded by the same element and at the same scale. However, this is not the case with graylevel structuring functions. We provide two examples of PDEs generating multiscale dilations by graylevel structuring functions: If K is the compact-support spherical function

$$K(x,y) = \begin{cases} \sqrt{1+x^2+y^2}, & x^2+y^2 \le 1 \\ -\infty, & x^2+y^2 > 1 \end{cases}$$

the dilation PDE becomes [17,84]

$$\delta_t = \sqrt{1+(\delta_x)^2+(\delta_y)^2}$$

For the infinite-support parabolic structuring function

$$K(x,y) = -a(x^2+y^2), \quad a > 0$$

the dilation PDE becomes [84]

$$\delta_t = [(\delta_x)^2 + (\delta_y)^2]/4a$$

All previous dilation (and erosion) PDEs can be unified using slope transforms. Specifically, let

$$K^\vee(a,b) \stackrel{\triangle}{=} \bigvee_{(x,y)\in \mathbb{R}^2} K(x,y) - (ax+by)$$

be the upper slope transform [25,48,49] of K, which is closely related to the Legendre-Fenchel conjugate of K [34,66]. Then, as discussed in [34,56], the rate of change of δ in scale is equal to the upper slope transform of the structuring function evaluated at the spatial gradient of δ:

$$\frac{\partial \delta}{\partial t} = K^\vee\left(\frac{\partial \delta}{\partial x}, \frac{\partial \delta}{\partial y}\right) \tag{7}$$

Similarly, the PDE generating the multiscale erosion by K is:

$$\frac{\partial \varepsilon}{\partial t} = -K^{\vee}\left(\frac{\partial \varepsilon}{\partial x}, \frac{\partial \varepsilon}{\partial y}\right)$$

All examined dilation and erosion PDEs are special cases of Hamilton-Jacobi equations, which are of paramount importance in physics. Such equations usually do not admit classic (i.e., everywhere differentiable) solutions. Generalized (viscosity) solutions of Hamilton-Jacobi PDEs have been extensively studied in Lions [43] and Crandall, Ishii and Lions [23]. Based on the theory of viscosity solutions, Heijmans and Maragos [34] have shown via slope transforms that, the multiscale dilation by a general upper-semicontinuous concave function is the viscosity solution of the Hamilton-Jacobi dilation PDE (7).

3. Distance Transforms

3.1. Distance transforms and wave propagation

For binary images, the distance transform is a compact way to represent multiscale dilations and erosions by convex polygonal structuring elements whose shape depends upon the norm used to measure distances. Specifically, a binary image can be divided into the foreground set $S \subseteq \mathbb{R}^2$ and the background set $S^c = \{(x, y) : (x, y) \notin S\}$. For shape analysis of an image object S, it is often more useful to consider its inner distance transform, by using S as the domain to measure distances from its background. However, for the applications discussed herein, we need to view S as a region marker, or a source, emanating a wave that will propagate away from it into the domain of S^c. Thus, we define the *outer distance transform* of a set S, with respect to the metric induced by some norm $||\cdot||_p$, $p = 1, 2, \ldots, \infty$, as the distance function

$$\text{dist}_p(S)(x, y) \stackrel{\triangle}{=} \bigwedge_{(v,w)\in S} ||(x - v, y - w)||_p \tag{8}$$

Thresholding the distance transform at level $r > 0$, and obtaining the corresponding level set, yields the morphological dilation $\oplus$ of S by the ball B_p at scale r:

$$S \oplus rB_p = \{(x, y) : \text{dist}_p(S)(x, y) \geq r\}$$

The boundaries of these dilations are the wavefronts of the distance propagation. Multiscale erosions of S can be obtained from the outer distance transform of S^c.

In addition to being a compact representation for multiscale erosions and dilations, the distance transform has found many applications in image analysis and computer vision. Examples include smoothing, skeletonization, size distributions, shape description, object detection and recognition, segmentation, and path finding [13, 14, 60, 65, 67, 68, 86, 88]. Thus, many algorithms have been developed for its computation.

Let now $p = 2$. Using Huygen's construction [15], the boundaries of multiscale dilations/erosions by disks can also be viewed as the wavefronts of a wave initiating from the

original image boundary and propagating with constant normal speed, i.e., in a homogeneous medium. Thus, the distance function has a minimum time-of-arrival interpretation [13] and its isolevel contours coincide with those of the wave phase function. Points where these wavefronts intersect and extinguish themselves (according to Blum's grassfire propagation principle [13]) are the points of the Euclidean skeleton (medial) axis of S [12, 13]. Overall, the Euclidean distance function $\text{dist}_2(S)$ is the weak solution of the following nonlinear PDE

$$\begin{aligned} ||\nabla E(x,y)||_2 &= 1, \quad (x,y) \in S^c \\ E(x,y) &= 0, \quad (x,y) \in S \end{aligned}$$

This is a special case of the eikonal PDE $||\nabla E(x,y)||_2 = \eta(x,y)$, which corresponds to wave propagation in heterogeneous media and whose solution E is a weighted distance function, where the weights $\eta(x,y)$ are inversely proportional to the varying propagation speed [42, 69, 85].

3.2. Distance transforms as infimal convolutions

If we consider the $0/\infty$ indicator function of S

$$\text{ind}(S)(x,y) \stackrel{\triangle}{=} \begin{cases} 0, & (x,y) \in S \\ +\infty, & (x,y) \notin S \end{cases}$$

and the norm structuring function

$$g_p(x,y) = ||(x,y)||_p$$

it follows that

$$\text{dist}_p(S) = \text{ind}(S) \oplus' g_p \tag{9}$$

Hence, the distance transform can be obtained from the infimal convolution of the indicator function of the set with the norm function [66, 81].

Since the relative ordering of distance values does not change if we raise them to a positive power $m > 0$, it follows from (9) that

$$[\text{dist}_p(S)]^m = \text{ind}(S) \oplus' (g_p)^m.$$

If $m = 2$ and we use the Euclidean norm ($p = 2$), the previous result implies that [83]

$$[\text{dist}_2(S)]^2 = \text{ind}(S) \oplus' (g_2)^2 \tag{10}$$

Note that, in this case, $(g_2(x,y))^2 = ||(x,y)||_2^2 = x^2 + y^2$ is a convex parabola.

3.3. Euclidean distance transform

To obtain isotropic distance propagation, the Euclidean distance transform (i.e., using the norm $||\cdot||_2$ in (8)) is desirable because it gives multiscale morphology with the disk as the structuring element. However, the Euclidean distance transform of discrete images has a significant

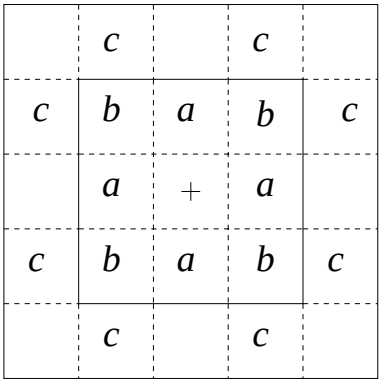

Figure 1 Masks of distance steps for chamfer metrics using 3×3 and 5×5 neighborhoods for local distance propagation. The unmarked pixels are not used.

computational complexity. Thus, various techniques are used to obtain approximations to the Euclidean distance transform at a lower complexity. Examples include [24, 79, 87]. Another approach [83] is based on the exact computation of the squared Euclidean distance transform via infimal convolution of the binary image by a parabolic structuring function, as in (10). The complexity of this exact approach can be significantly reduced using dimensional decomposition of the 2D parabolic structuring function, by expressing it either as the dilation of two 1D quadratic structuring functions [83] or as the dilation of several 3×3 kernels that yields a truncation of the 2D parabola [36].

3.4. Chamfer distance transforms

Discrete approximations to Euclidean distance transforms, especially of binary images, have been studied extensively in image processing. Their early theory was developed by Rosenfeld and Pfaltz [67, 68], based on either sequential or parallel operations. Later generalizations, including improved approximations to the Euclidean distance, were developed by Borgefors [14] based on 'chamfer' metrics. The general chamfer distance transform is obtained by *propagating local distances* within a small neighborhood. The masks of fixed local distance steps are shown in Fig. 1. For a 3×3-pixel neighborhood, if (a, b) are the horizontal and diagonal distance steps, respectively, the outer (a, b) chamfer distance transform of a discrete set $S \subseteq \mathbb{Z}^2$ can be obtained via the following sequential [14, 67] computation[2]

$$\begin{aligned} u_n[i,j] \;=\; \min(&u_n[i-1,j]+a,\, u_n[i,j-1]+a, \\ &u_n[i-1,j-1]+b,\, u_n[i-1,j+1]+b,\, u_{n-1}[i,j]) \end{aligned} \tag{11}$$

Starting from $u_0 = \mathrm{ind}(S)$ as the $0/\infty$ indicator function of S, two passes ($n = 1, 2$) of the 2D recursive erosion (11) suffice to compute the chamfer distance transform of S, if S^c is bounded

[2] By $f[x]$, we denote functions f with integer argument $x \in \mathbb{Z}^d$.

(a) (b) (c)

Figure 2 Sequential computation of the chamfer distance transform with optimal distance steps in a 3×3 mask. (a) Original binary image (450×450 pixels). (b) Result after forward scan. (c) Final result after backward scan (in (b) and (c), the distances are displayed as intensity values modulo a constant).

and simply connected.[3] During the first pass, the image is scanned from top-left to bottom-right using the 4-point non-symmetric half-plane submask of the 3×3 neighborhood of Fig. 1. During the second pass, the image is scanned in the reverse direction using the reflected submask of distance steps. The final result $u_2[i,j]$ is the outer (a,b) chamfer distance transform of S, evaluated at points of $\mathbb{Z}^2$. An example of the three images, u_0, u_1, and u_2, is shown in Fig. 2. The same final result can also be obtained via parallel or queue-based algorithms [68, 86].

The above chamfer distances (with a 3×3 mask) can also be obtained via the (a,b) *chamfer norm*

$$||(x,y)||_{a,b} \stackrel{\triangle}{=} \max(|x|,|y|)a + \min(|x|,|y|)(b-a)$$

The unit ball, corresponding to this chamfer norm, is a symmetric octagon. By using this chamfer norm, in place of the general norm $||\cdot||_p$ in (8), the outer (a,b) chamfer distance transform of S can be expressed as

$$\text{dist}_{a,b}(S)(x,y) = \bigwedge_{(v,w)\in S} ||(x-v, y-w)||_{a,b}$$

Note that, the above two equations apply to sets S and points (x,y), both in the continuous plane $\mathbb{R}^2$ as well as in the discrete plane $\mathbb{Z}^2$.

Selecting the steps a, b under certain constraints leads to an infinite variety of chamfer metrics based on a 3×3 mask. Two well-known, and easily computable special cases, called the cityblock and chessboard metrics [67], are the choices for (a,b) to be $(1,\infty)$ or $(1,1)$, which corresponds to the chamfer ball being a rhombus or square, respectively. These two choices give the poorest discrete approximations to the Euclidean distance (and to multiscale morphology with a disk structuring element), with errors reaching 41.4% and 29.3%, respectively. Using

[3] If S^c contains holes, we need a constrained distance transform [26].

Euclidean steps, $(a, b) = (1, \sqrt{2})$ yields a 7.61% maximum error. Thus, a major design goal is to reduce the approximation error between the chamfer distances and the corresponding Euclidean distances [14]. A suitable error criterion is the *maximum absolute error* (MAE) between a unit chamfer ball and the corresponding unit disk [19, 86]. The optimal steps obtained in Butt and Maragos [19], by minimizing this MAE, are $a = 0.9619$ and $b = 1.3604$, which give a 3.957% maximum error. In practice, and for faster implementation, integer-valued distance steps A and B are used, and the computed distance transform is divided by a normalizing constant k which can be real-valued. We refer to such a metric as $(a, b) = (A, B)/k$. Using two decimal digits for truncating optimal values and optimizing the triplet (A, B, k) for the smallest possible error as in [19], we get $A = 70$, $B = 99$, and $k = 72.77$. The corresponding steps are

$$(a, b) = (70, 99)/72.77$$

yielding a 3.959% MAE. By working as above, for optimizing the steps $(a, b, c,)$ of chamfer distances with a 5×5 mask (see Fig. 1), the resulting integer approximation of the optimal steps is

$$(a, b, c) = (34, 48, 76)/34.45$$

yielding a 1.358% MAE. Henceforth, by 'optimal' chamfer distance transforms we mean using the optimal steps in the above two equations. See Fig. 3 and Fig. 4 for examples.

4. Curve Evolution

Consider, at time $t = 0$, an initial simple, smooth and closed planar curve $\gamma(0)$, which is propagated, for $t > 0$, along its normal vector field with speed V. Let this evolving curve (front) $\gamma(t)$ be represented by its position vector $\vec{C}(p, t) = (x(p, t), y(p, t))$ and be parameterized by $p \in J$, so that its interior is on the left in the direction of increasing p. The metric (henceforth in the paper we use $||\cdot|| = ||\cdot||_2$)

$$||\vec{C}_p|| = \sqrt{x_p^2 + y_p^2}$$

is the speed while traveling the curve, where $\vec{C}_p = \partial\vec{C}/\partial p$. If the curve is re-parameterized via its (Euclidean) *arc length parameter*

$$\ell(p, t) = \int_0^p ||\vec{C}_p(\xi, t)|| d\xi,$$

then $||\vec{C}_\ell|| = 1$. Let the angle formed by the *tangent vector* $\vec{C}_p$ and the x-axis be

$$\theta = \arctan(y_p/x_p)$$

The (Euclidean) *curvature* is

$$\kappa \stackrel{\triangle}{=} \frac{\partial\theta}{\partial\ell} = \frac{y_{pp}x_p - y_p x_{pp}}{(x_p^2 + y_p^2)^{3/2}}$$

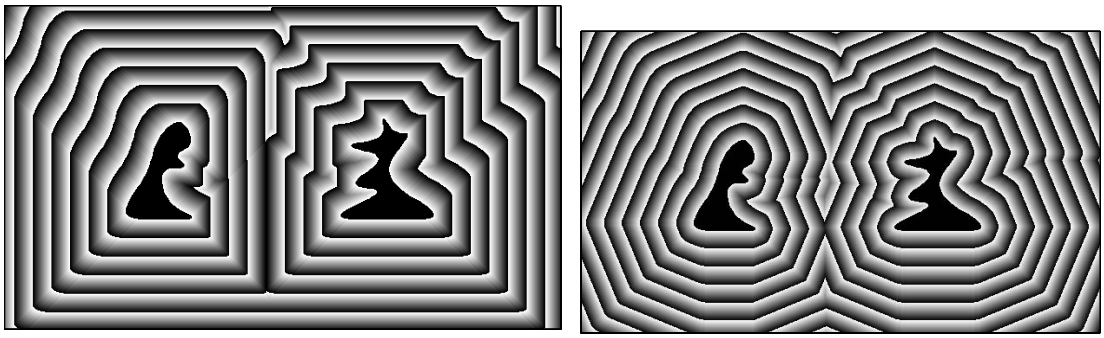

(a) (b)

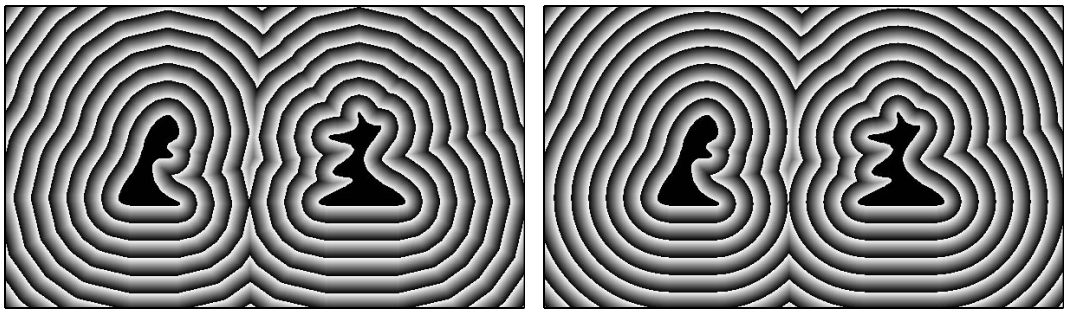

(c) (d)

Figure 3 Distance transforms of a binary image (the filled black region) obtained via: (a) (1,1) chamfer metric; (b) optimal 3×3 chamfer metric; (c) optimal 5×5 chamfer metric; (d) curve evolution (discussed in Section 4). In all these figures, the distances are displayed as intensities modulo a constant $h = 20$. All images have a resolution of 450×600 pixels.

A general front propagation law (flow) is

$$\frac{\partial \vec{C}(p,t)}{\partial t} = V\vec{N}(p,t) \tag{12}$$

with initial condition $\gamma(0) = \{\vec{C}(p,0) : p \in J\}$, where $\vec{N}(p,t)$ is the instantaneous unit *outward normal* vector at points on the evolving curve, and V is the *normal speed*

$$V \triangleq \vec{C}_t \cdot \vec{N}$$

with $\vec{C}_t = \partial\vec{C}/\partial t$. This speed may generally depend on local geometrical information, such as curvature, global image properties, or other factors independent of the curve. If $V = 1$ or

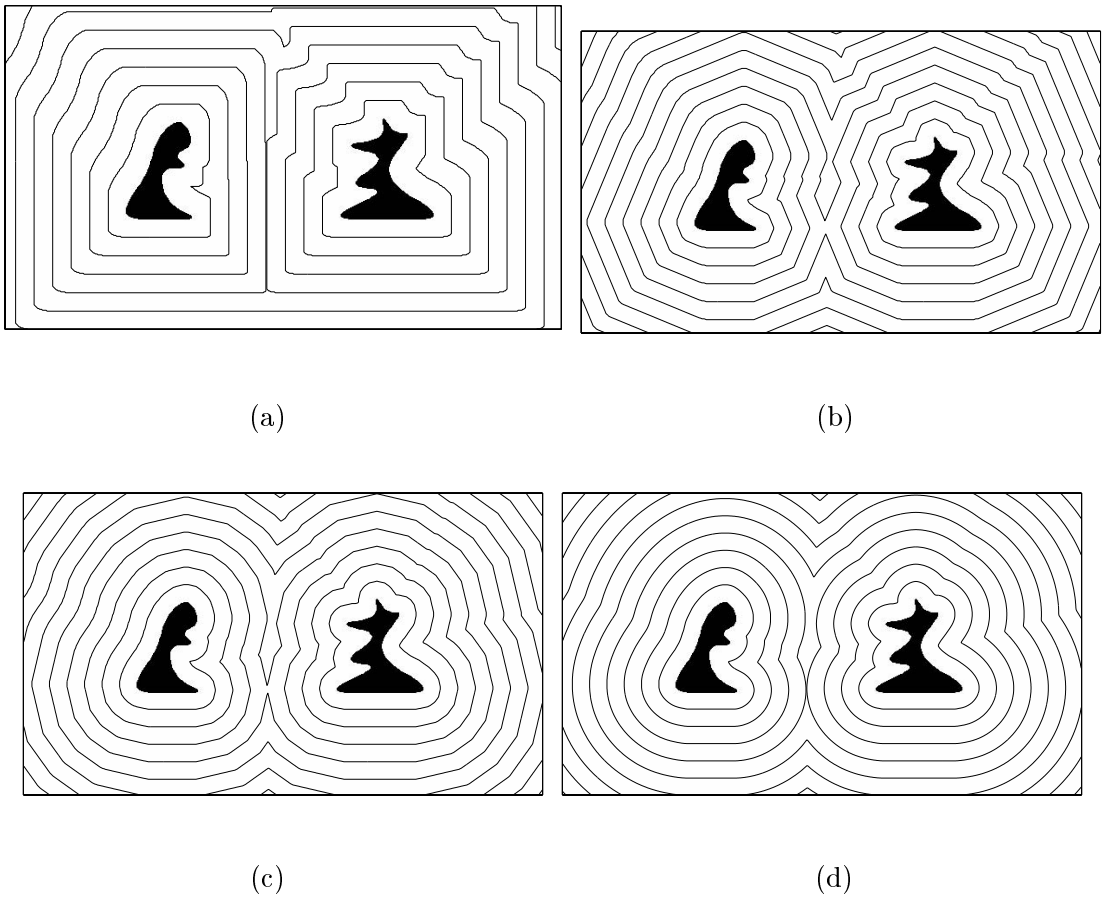

(a) (b)

(c) (d)

Figure 4 Multiscale dilations (at scales $t = nh$, $n = 1, 2, \ldots$) of a binary image (the filled black region), obtained by thresholding the corresponding distance transforms of Fig. 3 at isolevel contours whose levels are multiples of $h = 20$. In (a,b,c), the equivalent structuring elements for the dilations are the chamfer unit-scale polygons corresponding to the metrics used in Figs. 3(a,b,c), whereas in (d) the element is the disk.

$V = -1$, then $\gamma(t)$ is the boundary of the dilation or erosion of the initial curve $\gamma(0)$ by a disk of radius t.

4.1. Level set formulation: from curves to functions

To overcome the topological problem of splitting and merging, as well as numerical problems with the Lagrangian formulation (12), an Eulerian formulation was proposed by Osher and Sethian [62], where the original curve $\gamma(0)$ is first embedded in the surface of an arbitrary 2D Lipschitz continuous function $\phi_0(x, y)$, as its level set (contour line), at a constant level λ. For example, we can select $\phi_0(x, y)$ to be equal to the signed distance function from the boundary

of $\gamma(0)$:

$$\phi_0(x,y) = \begin{cases} \lambda, & (x,y) \in \gamma(0) \\ \lambda + \bigwedge\limits_{(v,w)\in\gamma(0)} ||(x-v, y-w)||, & (x,y) \in \text{interior}(\gamma(0)) \\ \lambda - \bigwedge\limits_{(v,w)\in\gamma(0)} ||(x-v, y-w)||, & (x,y) \in \text{exterior}(\gamma(0)) \end{cases}$$

Then, the evolving planar curve is embedded as a constant-level curve of an evolving space-time function $\phi(x,y,t)$:

$$\gamma(t) = \{(x,y) : \phi(x,y,t) = \lambda\}$$

The embedding can be equivalently expressed by

$$\phi(\vec{C}(p,t), t) = \lambda \tag{13}$$

where $\vec{C}(p,t)$ is the path in time of a fixed, but otherwise arbitrary, point on the front. We refer to the embedding function ϕ as the 'level function.' The constant level will be set to $\lambda = 0$ for our subsequent analysis, but it can be an arbitrary real number.

Geometrical properties of the evolving curve can be obtained from spatial derivatives of the level function. Thus, at any point on the front, the curvature and outward normal of the level lines can be found from ϕ; i.e.,

$$\begin{aligned} \vec{N} &= -\frac{\nabla\phi}{||\nabla\phi||} \\ \kappa &= -\text{div}(\frac{\nabla\phi}{||\nabla\phi||}) = \nabla \cdot \vec{N} \end{aligned}$$

The curve evolution PDE (12) induces a PDE generating its level function. This can be obtained by differentiating (13) with respect to t, which yields

$$\phi_t + \nabla\phi \cdot \vec{C}_t = 0 \tag{14}$$

This, in turn, gives the PDE governing the evolution of the level function:

$$\frac{\partial\phi}{\partial t} = V||\nabla\phi|| \tag{15}$$

with initial condition $\phi(x,y,0) = \phi_0(x,y)$. If $V = 1$, the above function evolution PDE is identical to the flat circular dilation PDE (5), by equating scale with time. Thus, we can view this specific dilation PDE as a special case of the general function evolution PDE (15), where all level sets expand in a homogeneous medium, with $V = 1$. Propagation in a heterogeneous medium, with $V = V(x,y) > 0$, will later lead to the eikonal PDE.

The function evolution PDE (15) makes all level curves $\{(x,y) : \phi(x,y,t) = \lambda\}$ of ϕ expand with normal speed V. This follows from (14) and (15); i.e.,

$$\vec{C}_t \cdot \nabla\phi = -\phi_t = -V||\nabla\phi|| \Longrightarrow \vec{C}_t \cdot \vec{N} = V$$

which, in turn, implies that $\vec{C}_t = V\vec{N}$ (assuming only normal speeds).

The above discussion has established the fact that differential curve evolution induces a similar differential evolution of a function whose level curves (at a constant level) are the evolving curves, and vice-versa. Let us view the evolution of the curve $\gamma(t)$ to a new curve $\gamma(t+\Delta t)$ at a later time as a set transformation Ψ, and the corresponding evolution of the level function ϕ as a function transformation ψ. Then, given that any (upper semicontinuous) function can be uniquely represented by its (closed) level sets, it follows that the set operator Ψ induces a function operator ψ by operating on all level sets of an input function and vice-versa. This approach, of building function operators from set operators, and vice-versa, through level sets, has been extensively studied and used in morphological image and signal analysis [33, 46, 51, 52, 76].

4.2. Curvature-dependent flow

Consider a curve evolving by means of (12), with $V = 1 - \epsilon\kappa$, $\epsilon \geq 0$. This velocity model has been studied extensively in Osher and Sethian [62] and Sethian [78], for general evolution of interfaces, and in Kimia et al. [37, 38], for shape analysis in computer vision. When $V = 1$, the curvature κ evolves according to [78]

$$\kappa_t = \epsilon\kappa_{\ell\ell} + \epsilon\kappa^3 - \kappa^2 \tag{16}$$

When $\epsilon > 0$, the front remains smooth. However, if $\epsilon = 0$, then (16) becomes $\kappa_t = -\kappa^2$, whose solution is $\kappa(p,t) = \kappa(p,0)/[1 + t\kappa(p,0)]$. Thus, when $V = 1$, the front's curvature will develop singularities and the front will develop corners (i.e., the curve derivatives will develop shocks – discontinuities) at finite time, if the initial curvature is anywhere negative. Two ways to continue the front beyond the corners are: (*i*) If the front is viewed as a geometric curve, then each point is advanced along the normal by a distance t, and hence a 'swallowtail' is formed beyond the corners by allowing the front to pass through itself. (*ii*) If the front is viewed as the boundary separating two regions, an *entropy condition* [78] is imposed to disallow the front to pass through itself. Namely, if the front is a propagating flame, then 'once a particle is burnt, it stays burnt' [78]. The same idea was also used by Blum [13] to model grassfire propagation, leading to the medial axis of a shape. It is equivalent to using Huygen's principle to construct the front as the set of points at distance t from the initial front. This can also be obtained from multiscale dilations of the initial front by disks of radii $t > 0$. Both the swallowtail and the entropy solutions are *weak solutions* [41]. See Fig. 5 for an example. This figure shows that, when $\epsilon > 0$, motion with curvature-dependent speed has a smoothing effect. Furthermore, the limit of the solution for the case when $V = 1 - \epsilon\kappa$, as $\epsilon \downarrow 0$, is the entropy solution for the case when $V = 1$ [78].

4.2.1. Mean curvature motion (Euclidean shortening flow)

Another important case of curve evolution is when $V = -\kappa$; then,

$$\vec{C}_t = -\kappa\vec{N} = \vec{C}_{\ell\ell} \tag{17}$$

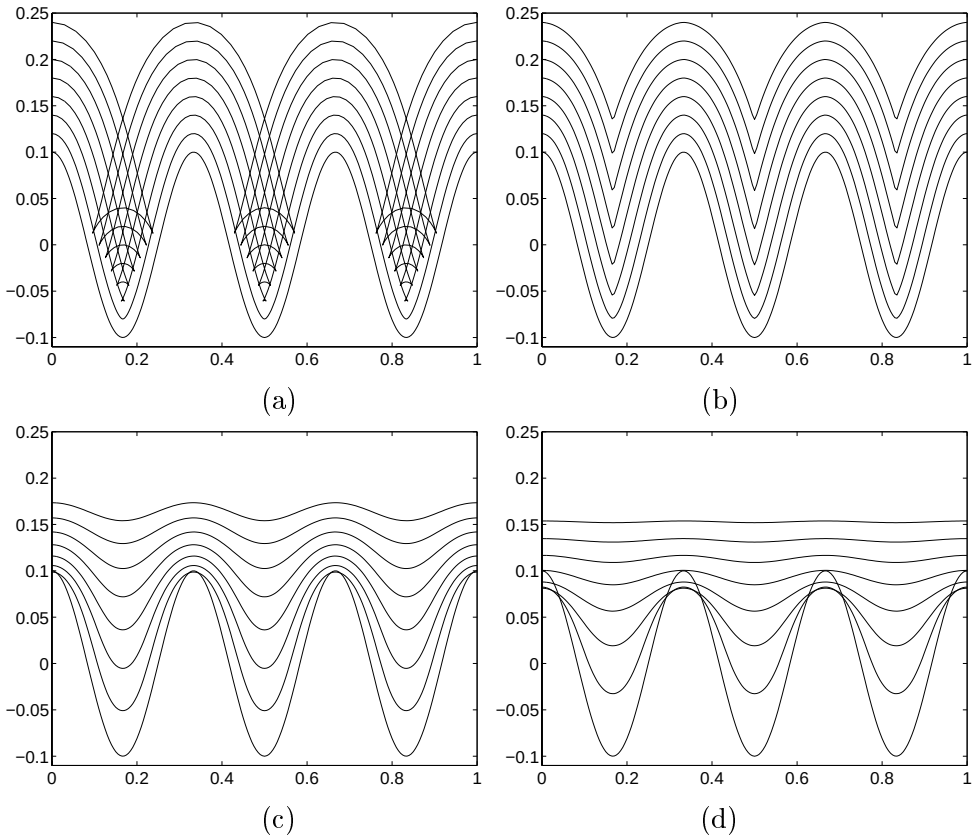

Figure 5 Evolution of the curve (signal graph) $(-p, \cos(6\pi p)/10)$, $p \in [0,1]$. Evolved curves are plotted from $t = 0$ to $t = 0.14$ at increments of 0.02. The numerical simulation for (b,c,d) is based on the Osher and Sethian algorithm, with $\Delta x = 0.005$ and Δt chosen small enough for stability. (a) $V = 1$, 'swallowtail' weak solution. (b) $V = 1$, entropy weak solution, with $\Delta t = 0.002$. (c) $V = 1 - 0.05\kappa$, with $\Delta t = 0.0002$. (d) $V = 1 - 0.1\kappa$, with $\Delta t = 0.0001$.

where ℓ is the arc length. This propagation model is known as *Euclidean geometric heat* (or *shortening*) *flow*, as well as *mean curvature motion*. Smooth simple curves, evolving by means of (17), remain smooth and simple and undergo some interesting phenomena: Their perimeter shrinks as fast as possible (Gage [29]). Any convex curve remains convex and shrinks to a round point (Gage and Hamilton [29, 30]). Furthermore, any non-convex curve converges first to a convex curve and from there it converges to a round point (Grayson [31]). See Fig. 6 for an example.

In contrast to the geometric heat flow (17), the linear heat flow

$$\vec{C}_t = \vec{C}_{pp} \Longleftrightarrow \begin{cases} x_t = x_{pp} \\ y_t = y_{pp} \end{cases}$$

evolves the curve in a way such that the coordinate functions $x(p,t)$ and $y(p,t)$ satisfy the heat

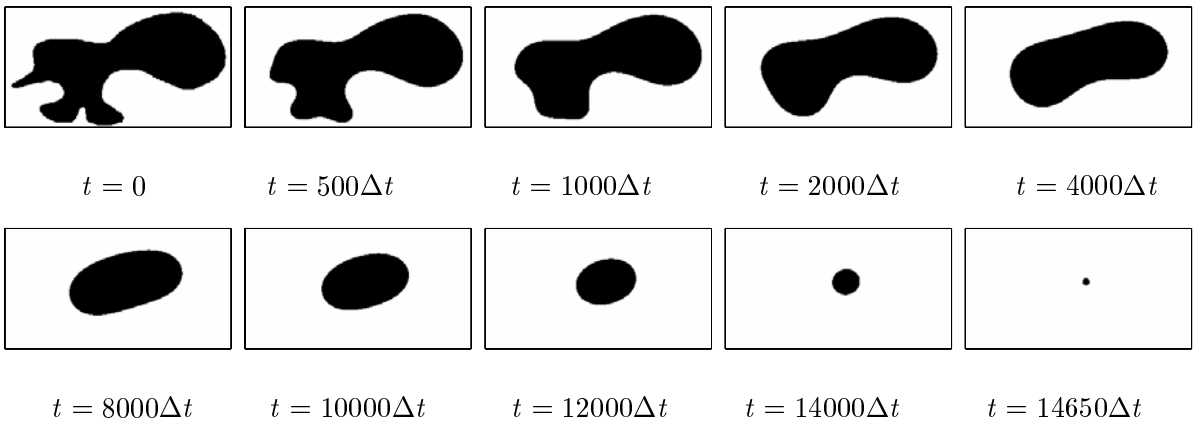

Figure 6 A non-convex shape collapsing to a round point under mean curvature flow ($V = -0.1\kappa$). The original shape vanishes after 14750 iterations ($\Delta t = 0.025$). All images have a resolution of 176×306 pixels.

diffusion PDE (1). Hence, the result can be obtained by multiscale linear convolutions of $x(p, 0)$ and $y(p, 0)$ with a Gaussian distribution of variance $2t$.

If the function $\phi(x, y, t)$ embeds a curve evolving by means of (17), as its level curve at a constant level, then it satisfies the evolution PDE

$$\phi_t = \mathrm{div}(\nabla\phi/||\nabla\phi||)||\nabla\phi|| = -\kappa||\nabla\phi||$$

This smooths all level curves by propagation under their mean curvature. It has many interesting properties and has been extensively studied by many groups of researchers, including Osher and Sethian [62, 78], Evans and Spruck [27], Chen, Giga and Goto [22], and Alvarez, Lions and Morel [4].

4.2.2. Affine shortening flow

Solutions of the Euclidean geometric heat flow (17) are invariant with respect to the group of Euclidean transformations (rotations and translations). Extending this invariance to affine transformations creates the *affine geometric heat flow* introduced by Sapiro and Tannenbaum [74]

$$\vec{C}_t = -\kappa^{1/3}\vec{N} = \vec{C}_{ss}$$

where s is the affine arc length, i.e., a re-parameterization of the curve such that

$$\det\left[\vec{C}_s\ \vec{C}_{ss}\right] = x_s y_{ss} - x_{ss} y_s = 1$$

Any smooth simple non-convex curve evolving by the affine flow (4.2.2) converges to a convex one and from there to an elliptical point [74].

4.2.3. Morphological representations of curvature flow

According to the representation theory developed by Maragos [45,46], every *translation-invariant* (TI), increasing, and *upper-semicontinuous* (u.s.c.) operator can be represented as a supremum of morphological erosions by its basis functions. Specifically, let ψ be a signal operator acting on $\mathrm{Fun}(\mathbb{E}, \overline{\mathbb{R}})$, i.e., the set of extended-real-valued functions defined on $\mathbb{E} = \mathbb{R}^d$ or $\mathbb{Z}^d$. If $\mathrm{Ker}(\psi) \stackrel{\triangle}{=} \{f : \psi(f)(x) \geq 0\}$ defines the *kernel* of ψ, then its *basis* $\mathrm{Bas}(\psi)$ is defined as the collection of the minimal (w.r.t. $\leq$) kernel functions. Then [46]:

$$\psi \text{ is TI, increasing, and u.s.c. } \Longrightarrow \psi(f) = \bigvee_{g \in \mathrm{Bas}(\psi)} f \ominus g$$

Dually, ψ can be represented as the infimum of dilations by functions in the basis of its dual operator $\psi^*(f) = -\psi(-f)$.

If the above function operator ψ is also flat (i.e., binary inputs yield binary outputs), with Ψ being its corresponding set operator, and commutes with thresholding, i.e.,

$$\Theta_\lambda[\psi(f)] = \Psi[\Theta_\lambda(f)], \quad \lambda \in \mathbb{R} \tag{18}$$

where $\Theta_\lambda(f) = \{x \in \mathbb{R}^d : f(x) \geq \lambda\}$ are the *threshold sets*[4] of f, then ψ is a supremum of flat erosions by the basis sets of its corresponding set operator Ψ [46]:

$$\psi(f) = \bigvee_{S \in \mathrm{Bas}(\Psi)} f \ominus S$$

where the basis[5] of the set operator is defined by

$$\mathrm{Bas}(\Psi) = \{S \subseteq \mathbb{E} : 0 \in \Psi(S) \text{ and } [0 \in \Psi(A) \text{ and } A \subseteq S] \Longrightarrow A = S\}$$

Equation (18) implies that [77, p. 188] the operator ψ is 'contrast-invariant' or 'morphologically-invariant,' which means that [2,32,76]

$$\psi(h(f)) = h(\psi(f))$$

where $h : \mathbb{R} \to \mathbb{R}$ is any monotone bijective function, and $h(f)$ is the image of f under h. Such a function h is called an 'anamorphosis' in [76,77], or a 'contrast-change' in [2,32].

The above morphological basis representations have been applied to various classes of operators, including morphological, median, stack, and linear filters [46,51,52]. Moreover, one can define translation-invariant, increasing and contrast-invariant filters as supremum (or infimum) of flat erosions (or dilations) by sets belonging to some basis $\mathbb{B}$. Catte, Dibos and Koepfler [20]

[4] The threshold sets have also been called 'horizontal cross-sections' in [76].

[5] The advantage of the morphological basis representations, over similar representations based on all elements of the (infinite-dimensional) kernel, for either set [55] or function [46] operators, is that the basis is finite, or finite-dimensional, for many useful operator classes.

selected as a basis the scaled version of a unit-scale isotropic basis (the set of all symmetric line segments of length 2)

$$\mathbb{B} = \{\{(x, y) : y = x\tan(\theta), |x| \leq 1\} : \theta \in [0, \pi)\}$$

and defined three types of multiscale flat operators:

$$\begin{aligned}
\mathcal{R}_t(f) &= \bigvee_{S\in\mathbb{B}} f \ominus \sqrt{2t}S \\
\mathcal{S}_t(f) &= \bigwedge_{S\in\mathbb{B}} f \oplus \sqrt{2t}S \\
\mathcal{T}_t(f) &= [\mathcal{I}_{2t}(f) + \mathcal{S}_{2t}(f)]/2
\end{aligned}$$

If these operators operate on a level function embedding a curve as one of its level lines, then this curve evolves according to the following three flows respectively [20]:

$$\begin{aligned}
\vec{C}_t &= -\max(\kappa, 0)\vec{N} \\
\vec{C}_t &= \min(\kappa, 0)\vec{N} \\
\vec{C}_t &= -\kappa\vec{N}
\end{aligned}$$

Hence, the above multiscale operators, which are sup-of-erosions and inf-of-dilations by linear segments in all directions, are actually curvature flows. A generalization of this result was obtained in Guichard and Morel [32], by assuming that $\mathbb{B}$ is any bounded and isotropic collection of planar sets. Furthermore, it has been shown in [8, 9, 32] that, by iterating n times a median filter, based on a window of scale r, we asymptotically converge (when $r \to 0$, $n \to \infty$, with $nr = t$) to the curvature flow. Note that, a median filter accepts a morphological basis representation [46, 52].

The above morphological representations deal with Euclidean curvature flow. Furthermore, by defining a unit-scale morphological basis $\mathbb{B}$ as a collection of convex symmetric sets invariant under the special linear group, it has been shown in [32] that n iterations of morphological flat operators at scale r, which are sup-of-erosions, inf-of-dilations, or their alternate compositions, converge (when $r \to 0$, $n \to \infty$, with $nr = t$) to the affine curvature flow.

4.3. Flows for morphological curve operations

As discussed previously, curve evolution with constant speed ($V = 1$) and the entropy condition, corresponds to Huygen's principle for 2D wavefront propagation, and equivalently, to multiscale set dilation by a unit disk. Now, if B is an arbitrary compact, convex, symmetric planar set of unit scale, imagine a generalized Huygen's rule for constructing the new wavefront $\gamma(t + \Delta t)$ by dilating the previous wavefront $\gamma(t)$ with $\Delta t B$. What is the corresponding curve evolution speed law? This has been answered in [6, 73] by focusing on the evolving curve. We shall provide an alternative proof, by focusing on the level function $\delta(x, y, t)$, which is a multiscale flat dilation

of the initial function $\delta(x, y, 0)$ by B. Hence, its generating PDE is given by (2). Viewing γ as the level curve

$$\gamma(t) = \{(x, y) : \delta(x, y, t) = \lambda\}$$

of the function δ at a constant level λ, and tracking the evolution of a point $\vec{C}$ on the front, yields

$$\delta(\vec{C}, t) = \lambda$$

Differentiating with respect to t, gives

$$\delta_t + \nabla\delta \cdot \vec{C}_t = 0$$

Then, from (2) and $\vec{N} = -\nabla\delta/||\nabla\delta||$, we obtain

$$\vec{C}_t = \frac{\text{sptf}(B)(\nabla\delta)}{||\nabla\delta||}\vec{N} = V\vec{N}, \quad V = \text{sptf}(B)(\vec{N})$$

where $\text{sptf}(B)$ is given in (3). Thus, the normal speed, required to evolve curves by dilating them with B, is simply the support function of B evaluated at the curve's normal.

4.4. Numerical algorithms

The level set method for curve evolution, with speeds

$$V = \beta - \epsilon\kappa$$

where β depends only on x, y, leads to the Hamilton-Jacobi PDE

$$\phi_t = \beta||\nabla\phi|| - \epsilon\kappa||\nabla\phi|| \tag{19}$$

If $\epsilon = 0$, such flows develop shocks, even if the initial data are smooth. After the formation of shocks, the solutions must be extended in a way that respects the original motion equation in conservation form and satisfies the entropy condition. Furthermore, it is desirable for any good discretization scheme to be highly accurate over smooth regions, reduce oscillations, and resolve shocks by confining them to a few grid points in a non-oscillatory way. By adapting the technology of conservative monotone discretization schemes for shock-producing PDEs of hyperbolic conservation laws [41], stable and shock-capturing numerical algorithms were developed in [62] for solving the above Hamilton-Jacobi PDEs. The main steps of such a first-order algorithm, by Osher and Sethian [62], to find an approximate solution to (19) when $\epsilon = 0$ and $\beta = \beta(x, y) > 0$ are:

$$\begin{aligned}
&\Phi^n_{i,j} = \text{approximation of } \phi(i\Delta x, j\Delta y, n\Delta t) \text{ on a grid. } V_{ij} = \beta(i\Delta x, j\Delta y).\\
&D_{+x}\Phi^n_{i,j} = (\Phi^n_{i+1,j} - \Phi^n_{i,j})/\Delta x, \quad D_{-x}\Phi^n_{i,j} = (\Phi^n_{i,j} - \Phi^n_{i-1,j})/\Delta x\\
&D_{+y}\Phi^n_{i,j} = (\Phi^n_{i,j+1} - \Phi^n_{i,j})/\Delta y, \quad D_{-y}\Phi^n_{i,j} = (\Phi^n_{i,j} - \Phi^n_{i,j-1})/\Delta y\\
&H = \sqrt{(0 \vee D_{-x}\Phi^n_{i,j})^2 + (0 \wedge D_{+x}\Phi^n_{i,j})^2 + (0 \vee D_{-y}\Phi^n_{i,j})^2 + (0 \wedge D_{+y}\Phi^n_{i,j})^2}\\
&\Phi^{n+1}_{i,j} = \Phi^n_{i,j} + V_{ij}H\Delta t, \quad n = 0, 1, 2, \ldots, (T_{max}/\Delta t)
\end{aligned} \tag{20}$$

where T_{max} is the maximum time (or scale) of interest, $\Delta x, \Delta y$ are the spatial grid spacings and Δt is the time (scale) step. For stability [62], the space/time steps must satisfy

$$(\Delta t/\Delta x + \Delta t/\Delta y)V_{ij} \leq 0.5$$

The dilation/erosion PDEs can be numerically solved via the above algorithm. Thus, by choosing fine grids (and possibly higher order terms), an arbitrarily low error (between signal values on the continuous plane and the discrete grid) can be achieved in implementing morphological operations involving disks as structuring elements. This is a significant advantage of the PDE approach, as observed in [6, 73]. Thus, curve evolution provides a geometrically better implementation of multiscale morphological operations with the disk-shaped structuring element. See Fig. 3 and Fig. 4 for an example.

If $\epsilon \neq 0$, a discretization scheme for the curvature term $\epsilon\kappa||\nabla\phi||$ in (19) must use central difference approximations to the derivatives involved.

Despite the many attractive features of the Osher and Sethian algorithm (such as robustness, subpixel accuracy, and its ability to handle topological problems via embedding), it also has the drawback that it cannot handle open curves and junctions and has the computational burden of embedding in a higher dimension. For curve evolution tasks, Tek and Kimia [82] have developed a numerical approach, based on propagating waves from boundary segments, inspired by Blum's grassfire propagation to find the skeleton. Their framework is Eulerian, numerically efficient, based on discrete wave fronts and discrete wave directions, and has been applied to distance transform computing and shock-based shape modeling.

5. Eikonal PDE

Many tasks for extracting information from visible images have been related to geometrical optics and wave propagation (for very small wavelengths) via the *eikonal* PDE [15, 71]

$$||\nabla E(x, y)|| = \eta(x, y)$$

where $\eta(x, y)$ is the refractive index field of a 2D optical medium. The scalar function $E(x, y)$, which is called the 'eikonal', has a gradient parallel to the optical rays, and its level sets are the wavefronts. Solving the eikonal can provide shape from shading, analog contour-based halftoning, and topographic segmentation of an image, by choosing the refractive index field $\eta(x, y)$ to be an appropriate function of the image brightness [35, 39, 49, 57, 61, 64, 75, 85].

The eikonal PDE can be seen as a stationary formulation of the embedding level function evolution PDE (15) with positive speed $V = \beta(x, y) = \beta_0/\eta(x, y) > 0$. Namely (see Osher and Sethian [62], Bardi and Falcone [7], and Falcone, Giorgi and Loreti [28]), if

$$T(x, y) = \inf\{t : \phi(x, y, t) = 0\}$$

is the minimum time at which the zero-level curve of $\phi(x, y, t)$ crosses (x, y), then

$$||\nabla T(x, y)|| = \frac{1}{\beta(x, y)}$$

Setting $E = \beta_0 T$ leads to the eikonal PDE.

Next, we outline two ways of solving the eikonal PDE and then discuss some of its applications especially in segmentation.

5.1. Weighted distance transform (WDT) as solution of the eikonal PDE

The solution of the eikonal PDE can be viewed as a *weighted distance function* whose value at each pixel is the optical length between that pixel and the light sources along a path of minimal optical length (see Born and Wolf [15], Levi and Montanari [42], Verbeek and Verwer [85], Rouy and Tourin [69], Kimmel, Kiryati and Bruckstein [39], and Maragos [49]). The *optical length* of any path is obtained by integrating the refractive index field $\eta(x, y)$ along this path and is proportional to the time required for light to travel this path. Thus, we can view the solution $E(x, y)$ of the eikonal PDE as a *Weighted Distance Transform* (WDT) whose values at each pixel give the minimum distance from the light sources weighted by the gray values of the refractive index field. Next, we outline two numerical methods for computing WDTs and discuss some of their implementations.

5.1.1. WDT based on chamfer metrics

Let $f[i, j] \geq 1$ be a sampled nonnegative graylevel image, and let us view it as a discrete refractive index field. Also, let S be a set of reference points, or the 'sources' of some wave, or the location of the wavefront at time $t = 0$. The discrete WDT finds, at each pixel $P = (i, j)$, the smallest sum of values of f over all possible discrete paths connecting P to the sources S. It can also be viewed as a procedure of finding paths of minimal 'cost' among nodes of a weighted graph, or as discrete dynamic programming. It has been extensively used in image analysis problems, such as minimal path finding, weighted distance propagation, graylevel image skeletonization, and geodesics; examples include [42, 57, 70, 80, 86].

The above discrete WDT can be computed sequentially by running a 2D min-sum difference equation, like in (11), that implements the chamfer distance transform of binary images, but with spatially-varying coefficients proportional to the gray image values [70, 85]:

$$\begin{aligned} u_n[i, j] = \min\{ & u_n[i-1, j] + af[i, j], \\ & u_n[i, j-1] + af[i, j], u_n[i-1, j-1] + bf[i, j], \\ & u_n[i-1, j+1] + bf[i, j], u_{n-1}[i, j]\} \end{aligned} \tag{21}$$

where $u_0 = \mathrm{ind}(S)$ is the $0/\infty$ indicator function of the source set S. Starting from u_0, a sequence of functions u_n is iteratively computed, by running (21) over the image domain in a forward scan, for even n, whereas, for odd n, an equation as in (21), but with a reflected coefficient mask, is run in a backward scan. In the limit $n \to \infty$, the final WDT u_∞ is obtained. In practice, this limit is reached after a finite number of passes. The number of iterations required for convergence depends on both the sources and the gray values. There are also other faster implementations using queues (see [57, 85]). The final transform is a function of the source set, the index field, and the norm used for horizontal distances.

The above WDT, based on discrete chamfer metrics, is shown in Verbeek and Verwer [85] and in Maragos [49] to be a discrete approximate solution of the eikonal PDE.

The constants a and b are the distance steps by which the planar chamfer distances are propagated within a 3×3 neighborhood. The propagation of the local distances (a, b) starts at the points of sources S and moves with speed $V = \beta(i\Delta x, j\Delta y) = \beta_0 / f[i, j]$. If f is a binary image, then the propagation speed is uniformly equal to one, and the solution of the above difference equation (after convergence) yields the discrete chamfer distance transform of S [14]. To improve the WDT approximation to the eikonal PDE's solution, we can optimize (a, b) so that the error is minimized between the planar chamfer distances and Euclidean distances. Using a neighborhood larger than 5×5, we can further reduce the approximation error, but at the cost of an even slower implementation. However, larger neighborhood masks cannot be used with WDTs because they give erroneous results, since the large masks can bridge over a thin line that separates two segmentation regions. Overall, this chamfer metric approach to WDT is fast and easy to implement, but, due to the required small neighborhoods, is not isotropic and cannot achieve high accuracy.

5.1.2. WDT based on curve evolution

In this approach, at time $t = 0$, the boundary of each source is modeled as a curve $\gamma(0)$, which is then propagated with normal speed $V = \beta(x, y) = \beta_0 / \eta(x, y)$. The propagating curve $\gamma(t)$ is embedded as the zero-level curve of a function $\phi(x, y, t)$, where $\phi(x, y, 0) = \phi_0(x, y)$ is the signed (positive in the curve interior) distance from $\gamma(0)$. The function ϕ evolves according to the PDE

$$\frac{\partial \phi}{\partial t} = \beta(x, y) ||\nabla \phi|| \tag{22}$$

which corresponds to curve evolution in a heterogeneous medium with position-dependent speed $\beta > 0$, or equivalently to a successive front dilation by disks with position-varying radii $\beta(x, y)\Delta t$. This is a time-dependent formulation of the eikonal PDE [28, 62]. It can be solved via the Osher and Sethian numerical algorithm (20). The value of the resulting WDT, at any pixel (x, y) of the image, is the time it takes for the evolving curve to reach this pixel, i.e., the smallest t such that $\phi(x, y, t) \geq 0$. This continuous approach to WDT can achieve sub-pixel accuracy, as investigated in [39].

In the applications of the eikonal PDE examined in this paper, the global speed function $\beta(x, y)$ is everywhere positive. In such cases, the computational complexity of Osher and Sethian's level set algorithm (which can handle sign changes in the speed function) can be significantly reduced by using Sethian's *fast marching algorithm* [1, 78], which is designed to solve the corresponding stationary formulation of the eikonal PDE, i.e., $||\nabla T|| = 1/\beta$. There are also other types of numerical algorithms for solving stationary eikonal PDEs; e.g., Rouy and Tourin [69] have proposed an efficient iterative algorithm for solving $||\nabla E|| = \eta$.

5.1.3. Implementations of WDT algorithms

As we have explained in previous sections, each discrete distance transform, i.e., computation of a distance function over a discretized image, can be viewed as an approximation to the solution of the eikonal PDE with boundary conditions at the sources. Two types of distance transforms examined in this paper are those based on chamfer metrics and those based on curve evolution; the latter are implemented using the fast marching technique. A general distance transform is a global operator because its value at any pixel may depend upon the whole image information. Thus, there are many approaches to implement each distance transform which could be classified as being sequential, or parallel, or using special data structures.

The usage of special data structures aims at making the algorithm as fast as possible by processing each pixel only once or as few times as possible during the distance propagation from (processed) pixels with known values to (unprocessed) pixels with unknown values. Specifically, among all unprocessed pixels, if the pixel with minimum distance value is processed first, it will result in assigning to its neighbor pixels distance values higher than its own; hence, it will not be processed again. To ensure such 'in-order' processing of pixels, researchers have used various data structures. Examples include the simple *queues* (of the FIFO type) used by Vincent [88] for various morphological image processing tasks, the *'buckets'* with priorities used by Verbeek and Verwer [85] for computing the WDT based on chamfer metrics, the *multiple hierarchical queues* used by Meyer [11,57] for the watershed transformation (which is equivalent to a WDT as explained later), and the *min-heap* used by Sethian and his coworkers [1,78] for implementing the fast marching technique.

Algorithms based on a *single* queue are very efficient for computing distance transforms of binary images using the chessboard or cityblock metric. However, they become very inefficient for computing general chamfer distance transforms (of binary or graylevel images) or other weighted distance transforms. The reason for this performance degradation is that, in the case of a general WDT, when a pixel is processed and it propagates its WDT value to its neighbors, the neighbors are assigned different values. These pixels with different WDT values travel together on a single queue, but they cannot be processed together. Two elegant approaches to implement such complex types of distance propagation are the aforementioned multiple hierarchical queues used in digital watershed algorithms [11] and the min-heap used in fast marching [78]. In both approaches the new pixels are *sorted* and put in queues or nodes of the binary tree representing the min-heap according to their values. This ensures proper in-order processing of all pixels, thus yielding a monotonic progression of the evolving front. If N is the number of image pixels, the watershed computation based on multiple hierarchical queues has a complexity $O(N)$ if we exclude the time needed to shift pixels among queues, and the min-heap implementation of fast marching has a total complexity of $O(N \log N)$.

In our work, we have used a simple data structure, consisting of *two queues*, to implement WDTs based on chamfer metrics or on fast marching, for applications both with single sources as well as with multiple sources where triple points develop at the collision of several wavefronts. Our two-queue implementation of fast marching is summarized in Fig. 7. Our approach is a step

ahead of the simple one-queue approach but it falls short of the more efficient (but more difficult to program) multiple-queue or min-heap approach. We have two queues of the same length. At the start of the algorithm, starting pixels are put in the first queue. This queue is searched for minimum value. Then this queue is emptied out. If the pixel coming out has the minimum value, it is processed and its new neighbors are put on the other queue. If the pixel coming out has a value greater than the minimum, it is simply put on the other queue. More details about this algorithm can be found in Butt [18]. This two-queue approach avoids many of the problems of the one-queue approach and has the following advantages over the multiple queue approach: (i) It does *not* need the computationally expensive sorting step; instead, a simpler step of finding the minimum value of all pixels is used. (ii) It needs less computer memory. (iii) It is easier to code.

5.2. Ray tracing

Ray tracing in optical media is also modeled via the eikonal PDE. In Fig. 8, a plane (2D optical medium) is divided into two regions of different refractive indices, and the path of minimum optical length (least propagation time) is to be found between two points in these regions. There, we see that, the WDT based on curve evolution gives a better approximation of the true path of light than the WDTs based on the discrete (chamfer) distance transforms. This conclusion can be strengthened by looking at Fig. 9, which compares the estimated angles of incidence of the various methods for the ray tracing problem of Fig. 8, when they vary as functions of a variable ratio of refractive indices.

5.3. Gridless halftoning via the eikonal PDE

Inspired by the use in Schröder [75] of the eikonal function's contour lines for visually perceiving an intensity image $I(x,y)$, the work in Verbeek & Verwer [85] and especially in Pnueli & Bruckstein [64] attempts to solve the PDE

$$||\nabla E(x,y)|| = \text{constant} - I(x,y)$$

and create a binary *gridless* halftone version of $I(x,y)$ as the union of the level curves of the eikonal function $E(x,y)$. The larger the intensity value $I(x,y)$ is, the smaller the local density of these contour lines in the vicinity of (x,y). This eikonal PDE approach to gridless halftoning, which we call *eikonal halftoning*, is indeed very promising and can simulate various artistic effects, as shown in Figs. 10-11. There, we also see that the curve evolution WDT gives a smoother halftoning of the image than the WDTs based on chamfer metrics.

5.4. Watershed segmentation via the eikonal PDE

A powerful morphological approach to *image segmentation* is the *watershed transformation* [11, 89], which transforms an image $f(x,y)$ to the crest lines separating adjacent catchment basins that surround regional minima, or other 'marker' sets of feature points. In Najman and

Labels:

- **processed** pixels: All pixels under the markers; assign a distance transform value of zero to them.
- **active** pixels: Pixels at the outside boundary of the markers; their distance transform is known.
- **unprocessed** pixels: Pixels away from the markers.

Initialize:

- Put active pixels (at the boundary of all markers) in first queue of a two-queue data structure and compute their distance transform.

Loop:

- Find the minimum value of distance transform of all the pixels on the first queue.
- Check all pixels in the first queue for their values of distance transform.
- If the pixel under investigation has a distance transform value equal to the minimum
  - Mark the pixel as **processed**
  - Take all **unprocessed** neighbors of the pixel, mark them active, and put them on the second queue.
  - Solve the implicit quadratic equation

    $$\sqrt{(0 \vee D_{-x}T_{ij})^2 + (0 \wedge D_{+x}T_{ij})^2 + (0 \vee D_{-y}T_{ij})^2 + (0 \wedge D_{+y}T_{ij})^2} = \frac{1}{\beta}$$

    for all active pixels on the first queue and take the larger of the two solutions. Ignore the differentials involving **unprocessed** pixels.
- Else
  - Put the pixel on the second queue.
- Exchange the roles of the two queues and return to the top of the loop.

Figure 7 A two-queue implementation of WDT using fast marching for solving $||\nabla T|| = 1/\beta$.

Schmitt [61], it has been established that (in the continuous domain and assuming that the image is smooth and has isolated critical points), the continuous watershed transform is equivalent to finding a skeleton by influence zones with respect to a weighted distance function that uses points

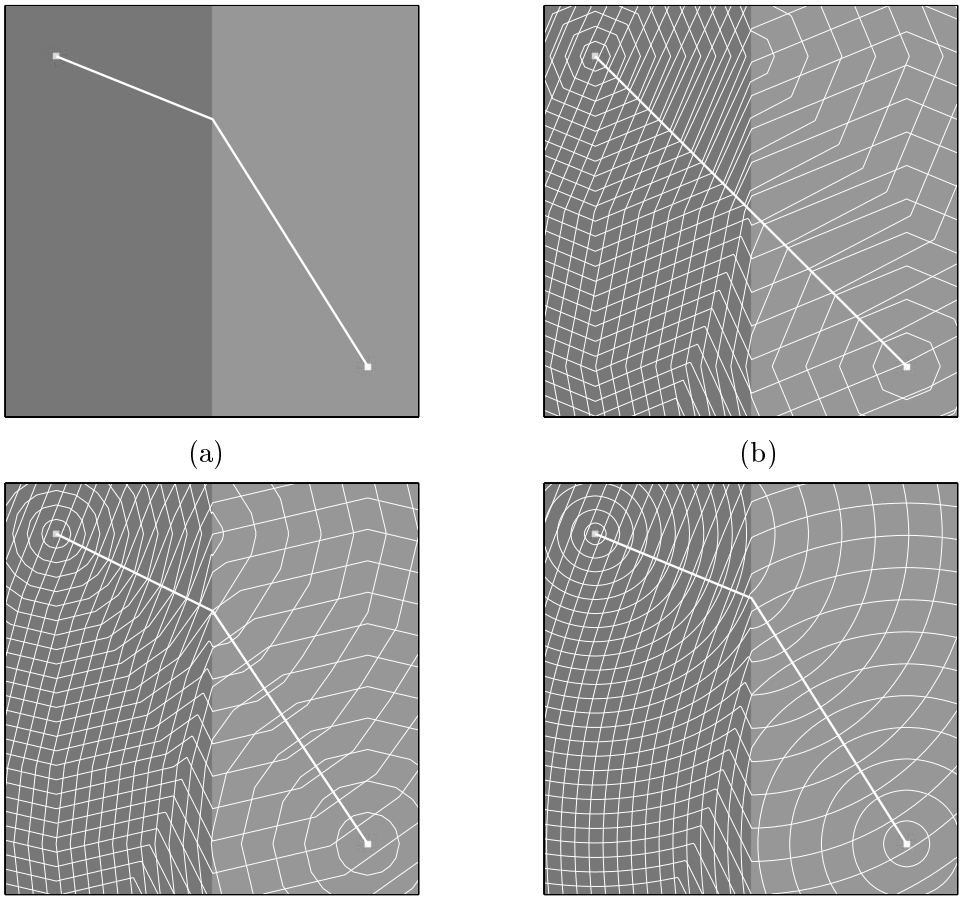

Figure 8 (a) Image of an optical medium consisting of two areas of different refractive indices and the correct path of the light ray (from Snell's law) between two points. The paths in (b,c,d) are found by using WDT based on: (b) optimal 3×3 chamfer metric; (c) optimal 5×5 chamfer metric; (d) curve evolution. In (b),(c),(d), the thin light contours show the wavefronts propagating from the two source points according to the various metrics. All images have a resolution of 320×320 pixels. The two point sources are located at pixels $(40, 40)$ and $(280, 280)$. The (graylevel) index ratio of the two regions is $5/3$.

in the regional minima of the image as sources[6] and $||\nabla f||$ as the field of indices, assuming that all minima have zero value. A similar result has been obtained by Meyer [58] for digital images. Furthermore, Meyer [57] has shown that an original discrete image I can be reconstructed from knowledge of $||\nabla I||$ via its discrete approximation by the erosion residual $I-(I\ominus B)$ (where B is a discrete disk) and of the image minima locations; he called this recovery of I from $I-(I\ominus B)$

[6] If other markers, different than the minima, are to be used as sources, then the homotopy of the function must be modified via morphological reconstruction to impose these markers as the only minima.

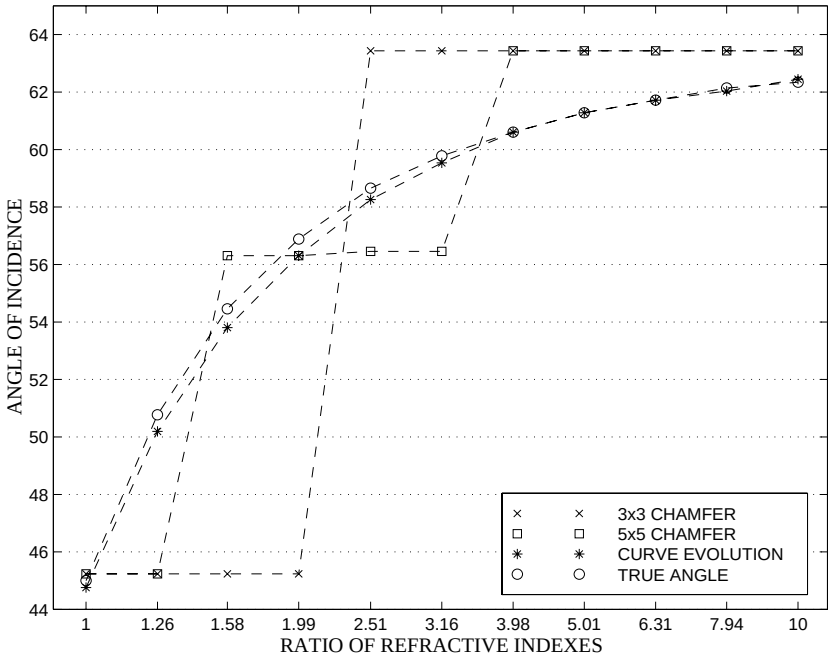

Figure 9 Variation of the estimated angles of incidence, as functions of the ratio of refractive indices, for the ray tracing problem of Fig. 8.

an 'integration.' Based on the above connections between the eikonal PDE and the watershed transform, it has been proposed in [58,61] to use existing efficient digital watershed algorithms for finding the solution to the eikonal equation.

In our work [50], we solve the above eikonal PDE model of watershed segmentation of an image-related function f, by finding a WDT via the curve evolution PDE (22), where the speed function β is proportional to $1/||\nabla f||$. Furthermore, we have compared the results of this new segmentation technique to the digital watershed algorithm via flooding [89] and to the eikonal PDE approach, solved via a discrete WDT based on chamfer metrics [58, 85]. In all three approaches, robust features are extracted first as markers of the regions. The original image I is then transformed to another function f, by smoothing via alternating opening/closing (either radial openings or openings by reconstruction), taking the gradient magnitude of the filtered image, and changing (via morphological reconstruction) the homotopy of the gradient image so that its only minima occur at the markers. The segmentation is done on the final outcome f of the above processing. Next we discuss two examples, shown in Figs. 12 and 14, of comparing the various discrete and continuous segmentation approaches in terms of their computational complexity and accuracy.

We have compared experimentally the complexity of the digital watershed flooding algorithm implemented as in [89] with that of our 2-queue implementation of fast marching adapted to handle multiple sources where triple points develop at the collision of several wavefronts. The

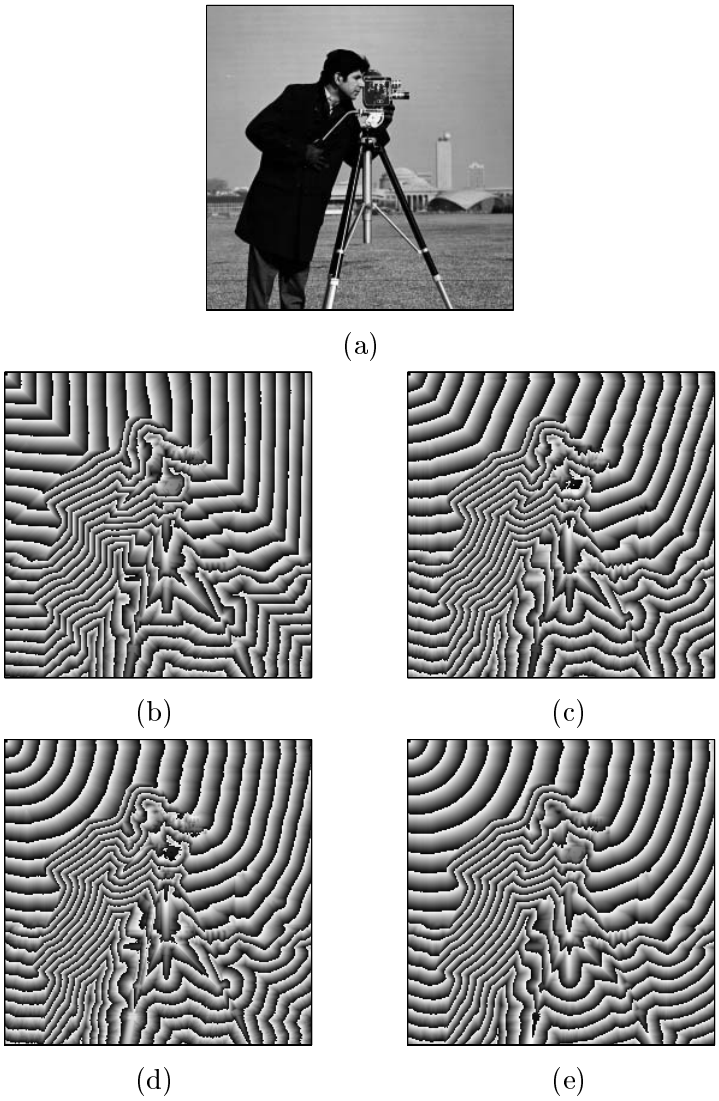

(a) (b) (c) (d) (e)

Figure 10 (a) Original CAMERAMAN image I (256×256 pixels). (b,c,d,e) show the weighted distance transforms (WDTs) of the 'negative' image $\max(I) - I$, where the light source was at the top left corner. The WDTs (displayed as intensities modulo a height, such that 25 waves exist per image) were obtained via: (b) (1,1) chamfer metric; (c) optimal 3×3 chamfer metric; (d) optimal 5×5 chamfer metric; (e) curve evolution.

experimental results on the images of Figs. 12 and 14 demonstrated that the complexity of our algorithm is affected by the number of markers used to segment the same image: more markers, slower execution. Thus, our PDE-based algorithm for segmenting the TEST image required smaller computation time than for segmenting the CAMERAMAN image, even if the former image is larger. For the CAMERAMAN image, the digital flooding algorithm was about 4

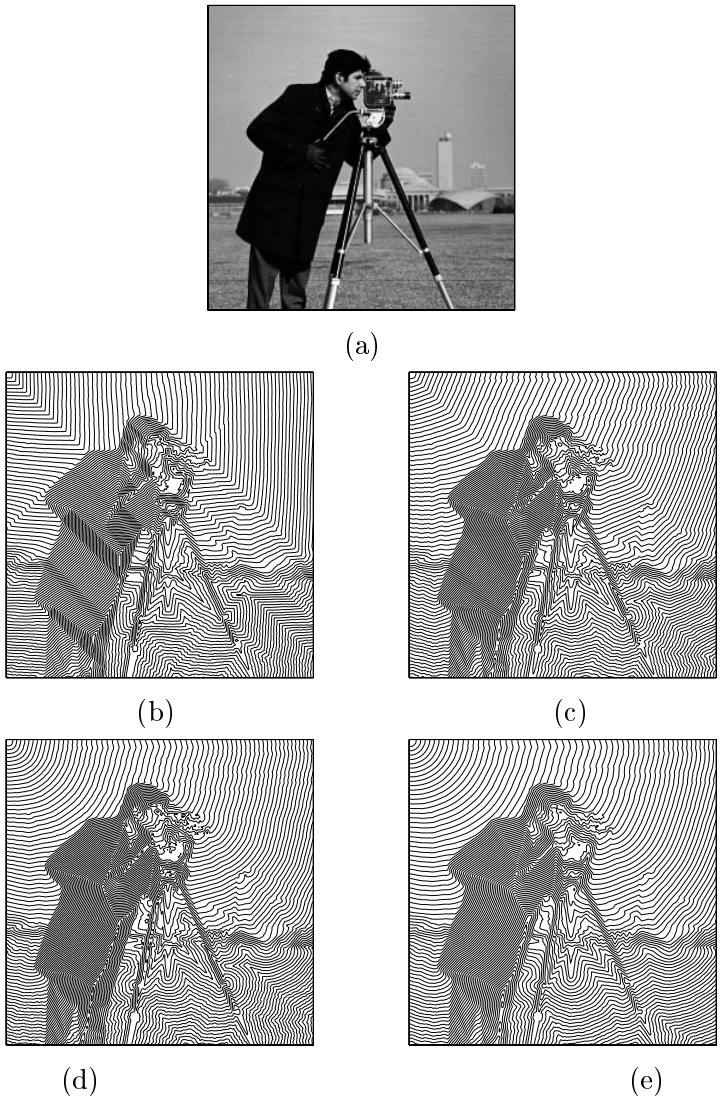

Figure 11 (a) CAMERAMAN image I. (b,c,d,e) show the eikonal halftonings of I, obtained by thresholding the weighted distance transform (WDT) of the negative image $\max(I) - I$. The light source and the methods for obtaining the WDT are identical to those of Fig. 10. In Figs. 11(b,c,d,e), 100 contour lines of the corresponding WDTs in Figs. 10(b,c,d,e), respectively, give a gridless halftoning of the original image.

times faster. However, for a few markers as in the TEST image, the execution times of the two algorithms seemed to be of the same order.

In the standard digital watershed algorithm via flooding [59, 89], the flooding at each level is achieved by a planar distance propagation that uses the chessboard metric. This kind of distance propagation is non-isotropic and could give wrong results, particularly for images with

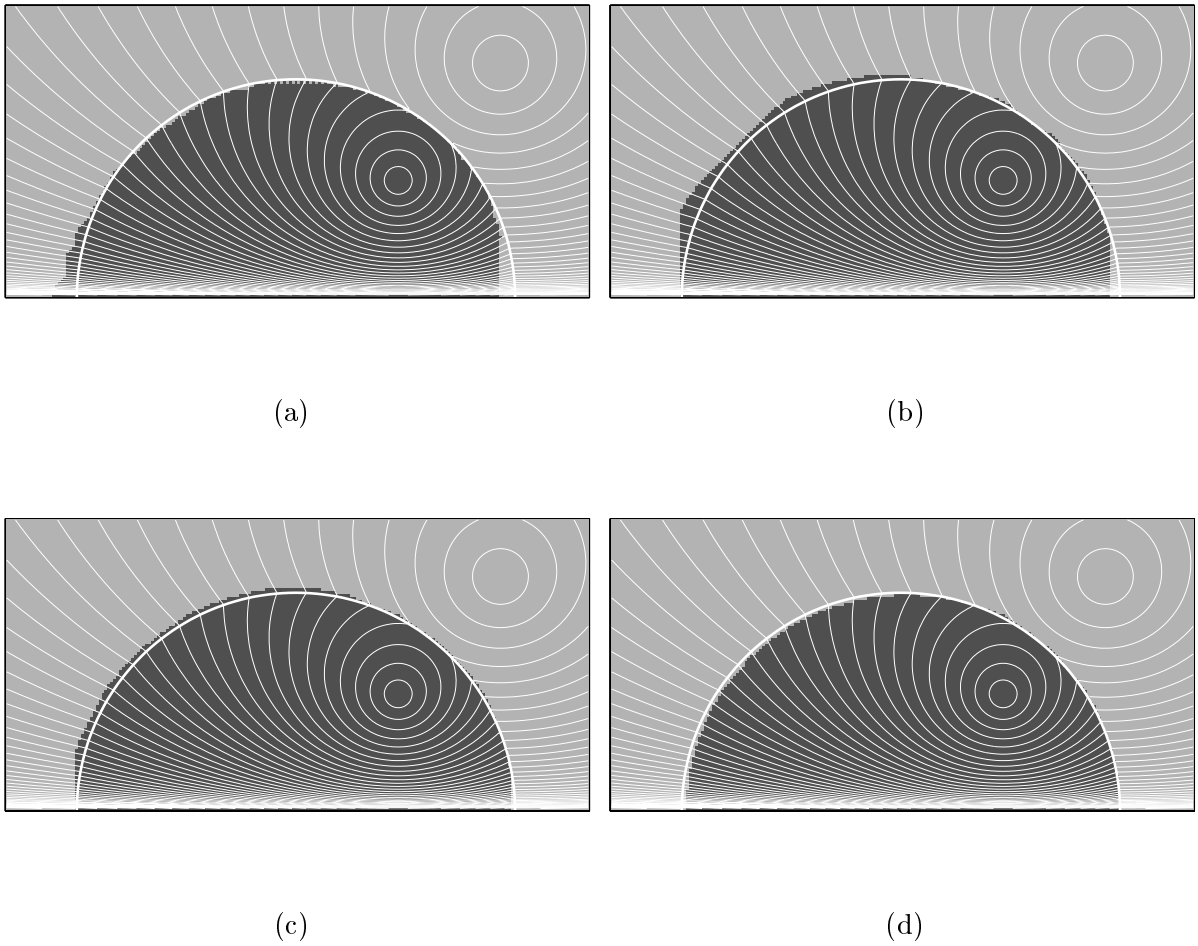

(a) (b)

(c) (d)

Figure 12 Performance of various segmentation algorithms on a TEST image (250×400 pixels). This image is the minimum of two potential functions. Its contour plot (thin bright curves) is superimposed on all segmentation results. Markers are the two source points of the potential functions. Segmentation results based on: (a) Digital watershed flooding algorithm. (b) WDT based on optimal 3×3 chamfer metric. (c) WDT based on optimal 5×5 chamfer metric. (d) WDT based on curve evolution (the thick bright curve shows the correct segmentation).

large plateaus, as we found experimentally. Eikonal segmentation, using WDTs based on chamfer metrics, improves this situation a little but not entirely. In contrast, for images with large plateaus/regions, segmentation via the eikonal PDE and curve evolution WDT gives results close to ideal. As Fig. 12 shows, compared on a test image that is difficult (because expanding wavefronts meet watershed lines at many angles ranging from being perpendicular to almost parallel), our continuous segmentation approach, based on the eikonal PDE and curve evolu-

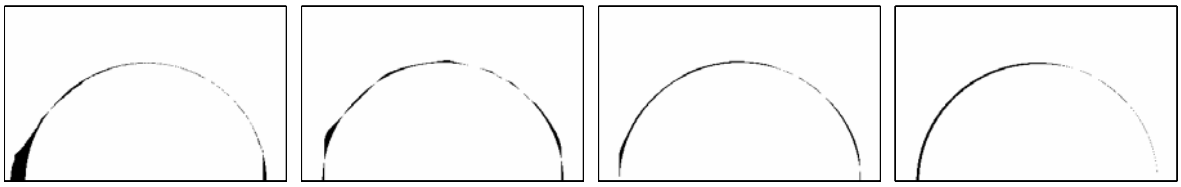

(a) (b) (c) (d)

Figure 13 Errors of the different segmentation approaches on the TEST image, shown as difference images between the segmented regions of Fig. 12 and the correct segmentation result (the true watershed line is a half circle). (a) Digital Flooding: 1.723% error. (b) 3×3 chamfer metric WDT: 1.195% error. (c) 5×5 chamfer metric WDT: 0.995% error. (d) Curve evolution WDT: 0.974% error.

tion, outperforms the discrete segmentation results (using either the digital watershed flooding algorithm or the discrete chamfer metric WDTs). Figure 13, which shows the corresponding segmentation errors, quantifies the superiority of the PDE approach for this test image. However, some real images, as in Fig. 14, may not contain many plateaus or only large regions, in which cases the digital watershed flooding algorithm may give comparable results to the eikonal PDE approach. In segmentation problems, where the image contains thin elongated regions surrounded by small-height edge walls, the digital flooding algorithm may be able to extract such regions, whereas the PDE approach may not be able to recover them completely. This happens because the small-height edges yield small image gradient values and hence large propagation speeds, which cause rapid flooding of such narrow regions. Of course, the fact that an eikonal PDE-based segmentation may not detect part, or all, of a thin elongated region could be an advantage in applications where such thin regions are noisy, or unreliable, and hence should not be detected by a robust segmentation scheme.

References

[1] D. Adalsteinsson, R. Kimmel, R. Malladi, and J.A. Sethian, "Fast Marching Methods for Computing the Solutions to Static Hamilton-Jacobi Equations", CPAM Report 667, Univ. California, Berkeley, 1996.

[2] L. Alvarez, F. Guichard, P.L. Lions, and J.M. Morel, "Axiomatization et nouveaux operateurs de la morphologie mathematique," *C. R. Acad. Sci. Paris*, pp. 265-268, t. 315, Serie I, 1992.

[3] L. Alvarez, F. Guichard, P.L. Lions, and J.M. Morel, "Axioms and Fundamental Equations of Image Processing," *Archiv. Rat. Mech.*, vol. 123 (3), pp. 199–257, 1993.

[4] L. Alvarez, P.-L. Lions, and J.-M. Morel, "Image Selective Smoothing and Edge Detection by Nonlinear Diffussion. II," *SIAM J. Numer. Anal.*, vol. 29, pp. 845–866, June 1992.

[5] L. Alvarez and J.M. Morel, "Formalization and computational aspects of image analysis," *Acta Numerica*, pp. 1–59, 1994.

(a) (b)

(c) (d)

Figure 14 (a) Original CAMERAMAN image (256×256 pixels), with markers placed within desired regions. (b) Gradient magnitude of filtered image. (c) Segmentation result(superimposed on original) from a digital watershed flooding algorithm. (d) Segmentation from eikonal PDE and curve evolution WDT.

[6] A. Arehart, L. Vincent and B. Kimia, "Mathematical Morphology: The Hamilton-Jacobi Connection," in *Proc. Int'l Conf. Comp. Vision*, pp. 215–219, 1993.

[7] M. Bardi and M. Falcone, "An Approximation Scheme For The Minimum Time Function," *SIAM J. Control and Optimization*, vol. 28, pp. 950-965, 1990.

[8] G. Barles and C. Georgelin, "A Simple Proof of Convergence for an Approximation Scheme

for Computing Motions by Mean Curvature," *SIAM J. Numer. Anal.*, vol. 32 (2), pp. 484–500, 1992.

[9] G. Barles and P. E. Souganidis, "Convergence of Approximation Schemes for Fully Nonlinear Second Order Equation," *Asympt. Anal.*, vol. 4, pp. 271–283, 1991.

[10] R. Bellman and W. Karush, "On the Maximum Transform," *J. Math. Anal. Appl.*, vol. 6, pp. 67–74, 1963.

[11] S. Beucher and F. Meyer, "The Morphological Approach to Segmentation: The Watershed Transformation," in *Mathematical Morphology in Image Processing*, E. R. Dougherty, Ed., Marcel Dekker, New York, 1993, pp.433–481.

[12] H. Blum, "A Transformation for Extracting New Descriptors of Shape," in Proceedings of the Symposium on *Models for the Perception of Speech and Visual Forms*, Boston, Nov. 1964, MIT Press, Cambridge, MA, 1967.

[13] H. Blum, "Biological shape and visual science (part I)," *J. Theor. Biol.*, vol. 38, pp. 205–287, 1973.

[14] G. Borgefors, "Distance Transformations in Digital Images," *Comp. Vision, Graphics, Image Process.*, vol. 34, pp. 344–371, 1986.

[15] M. Born and E. Wolf, *Principles of Optics*, Pergamon Press, Oxford, England, 1959 (1987 edition).

[16] R. W. Brockett and P. Maragos, "Evolution Equations for Continuous-Scale Morphology," *Proc. IEEE Int'l Conf. Acoust., Speech, Signal Processing*, San Francisco, CA, March 1992.

[17] R. Brockett and P. Maragos, "Evolution Equations for Continuous-Scale Morphological Filtering," *IEEE Trans. Signal Processing*, vol. 42, pp. 3377-3386, Dec. 1994.

[18] M. A. Butt, "Continuous and Discrete Approaches to Morphological Image Analysis with Applications: PDEs, Curve Evolution, and Distance Transform", Georgia Inst. Technology, Atlanta, USA, Mar. 1999

[19] M. A. Butt and P. Maragos. "Optimal Design of Chamfer Distance Transforms," *IEEE Trans. Image Processing*, vol. 7, pp. 1477-1484, Oct. 1998.

[20] F. Catte, F. Dibos and G. Koepfler, "A Morphological Scheme for Mean Curvature Motion and Applications to Anisotropic Diffusion and Motion of Level Sets," in *Proc. Int'l Conf. Image Processing*, Austin, TX, pp. 26–30, Nov. 1994.

[21] M. Chen and P. Yan, "A Multiscaling Approach Based on Morphological Filtering," *IEEE Trans. Pattern Anal. Mach. Intell.*, vol. 11, pp. 694–700, July 1989.

[22] Y.-G. Chen, Y. Giga and S. Goto, "Uniqueness and Existence of Viscocity Solutions of Generalized Mean Curvature Flow Equations," *J. Diff. Geometry*, vol. 33, pp. 749–786, 1991.

[23] M. G. Crandall, H. Ishii and P.-L. Lions, "User's Guide to Viscosity Solutions of Second Order Partial Differential Equations," *Bull. Amer. Math. Soc.*, vol. 27, pp. 1–66, July 1992.

[24] P.-E. Danielsson, "Euclidean Distance Mapping," *Comp. Graphics and Image Processing*, vol. 14, pp. 227–248, 1980.

[25] L. Dorst and R. van den Boomgaard, "Morphological Signal Processing and the Slope Transform," *Signal Processing*, vol. 38, pp. 79–98, July 1994.

[26] L. Dorst and P. W. Verbeek, "The Constrained Distance Transform: A Pseudo-Euclidean Recursive Implementation of the Lee-Algorithm," in Proc. EUSIPCO-86, *Signal Processing III: Theory and Applications* (I. T. Young et al., editors), Elsevier Sci. Publ. B.V., 1986, pp. 917-920.

[27] L. C. Evans and J. Spruck, "Motion of Level Sets by Mean Curvature. I," *J. Diff. Geom.*, vol. 33, pp. 635–681, 1991.

[28] M. Falcone, T. Giorgi and P. Loreti, "Level Sets of Viscocity Solutions: Some Applications to Fronts and Rendez-vous Problems," *SIAM J. Appl. Math.*, vol. 54, pp. 1335–1354, Oct. 1994.

[29] M. E. Gage, "Curve Shortening Makes Convex Curves Circular," *Invent. Math.*, vol. 76, pp. 357–364, 1984.

[30] M. Gage and R. S. Hamilton, "The Heat Equation Shrinking Convex Plane Curves," *J. Diff. Geom.*, vol. 23, pp. 69–96, 1986.

[31] M. A. Grayson, "The Heat Equation Shrinks Embedded Plane Curves to Round Points," *J. Diff. Geom.*, vol. 26, pp. 285–314, 1987.

[32] F. Guichard and J.-M. Morel, "Geometric Partial Differential Equations and Iterative Filtering," in *Mathematical Morphology and Its Applications to Image and Signal Processing* (H. Heijmans and J. Roerdink, Eds.), Kluwer Acad. Publ., 1998, pp. 127–138.

[33] H.J.A.M. Heijmans, *Morphological Image Operators*, Acad. Press, Boston, 1994.

[34] H.J.A.M. Heijmans and P. Maragos, "Lattice Calculus and the Morphological Slope Transform," *Signal Processing*, vol. 59, pp. 17–42, 1997.

[35] B.K.P. Horn, *Robot Vision*, MIT Press, Cambridge, MA, 1986.

[36] C. T. Huang and O. R. Mitchell, "A Euclidean Distance Transform Using Grayscale Morphology Decomposition," *IEEE Trans. Pattern Anal. Mach. Intellig.*, vol. 16, pp. 443–448, Apr. 1994.

[37] B. Kimia, A. Tannenbaum, and S. Zucker, "Toward a Computational Theory of Shape: An Overview," Proc. European Conf. on Comp. Vision, France, April 1990.

[38] B. Kimia, A. Tannenbaum, and S. Zucker, "On the Evolution of Curves via a Function of Curvature. I. The Classical Case," *J. Math. Anal. Appl.*, vol. 163, pp. 438-458, 1992.

[39] R. Kimmel, N. Kiryati, and A. M. Bruckstein, "Sub-Pixel Distance Maps and Weighted Distance Transforms," *J. Math. Imaging and Vision*, vol. 6, pp. 223-233, 1996.

[40] J. J. Koenderink, "The Structure of Images," *Biol. Cybern.*, vol. 50, pp. 363-370, 1984.

[41] P. D. Lax, "Hyperbolic Systems of Conservation Laws and the Mathematical Theory of Shock Waves," SIAM, Philadelphia, 1973.

[42] G. Levi and U. Montanari, "A Grey-Weighted Skeleton," *Information and Control*, vol. 17, pp. 62–91, 1970.

[43] P.-L. Lions, *Generalized Solutions of Hamilton-Jacobi Equations*, Pittman Publ., Boston, 1982.

[44] R. Malladi, J. A. Sethian, and B. C. Vemuri, "A Fast Level Set Based Algorithm for Topology-Independent Shape Modeling," *J. Math. Imaging and Vision*, vol. 6, pp. 269-289, 1996.

[45] P. Maragos, *A Unified Theory of Translation-Invariant Systems with Applications to Morphological Analysis and Coding of Images*, Ph.D. Thesis, Georgia Inst. Technology, Atlanta, June 1985.

[46] P. Maragos, "A Representation Theory for Morphological Image and Signal Processing," *IEEE Trans. Pattern Analysis and Machine Intelligence*, vol. 11, pp. 586–599, June 1989.

[47] P. Maragos, "Pattern Spectrum and Multiscale Shape Representation," *IEEE Trans. Pattern Anal. Mach. Intellig.*, vol. 11, pp. 701-716, July 1989.

[48] P. Maragos, "Morphological Systems: Slope Transforms and Max–Min Difference and Differential Equations," *Signal Processing*, vol. 38, pp. 57–77, July 1994.

[49] P. Maragos, "Differential Morphology and Image Processing" *IEEE Trans. Image Processing*, vol. 78, pp. 922–937, June 1996.

[50] P. Maragos and M. A. Butt, "Advances in Differential Morphology: Image Segmentation via Eikonal PDE and Curve Evolution and Reconstruction via Constrained Dilation Flow," in *Mathematical Morphology and Its Applications to Image and Signal Processing* (H. Heijmans and J. Roerdink, Eds.), Kluwer Acad. Publ., 1998, pp. 167–174.

[51] P. Maragos and R. W. Schafer, "Morphological Filters – Part I: Their Set-Theoretic Analysis and Relations to Linear Shift-Invariant Filters," *IEEE Trans. Acoust., Speech, and Signal Processing*, vol. 35, pp. 1153–1169, Aug. 1987.

[52] P. Maragos and R. W. Schafer, "Morphological Filters – Part II: Their Relations to Median, Order-Statistic, and Stack Filters," *IEEE Trans. Acoust., Speech, and Signal Processing*, vol. 35, pp. 1170–1184, Aug. 1987. "Corrections," *IEEE Trans. ASSP*, vol. 37, no. 4, p. 597, Apr. 1989.

[53] P. Maragos and R. W. Schafer, "Morphological Systems for Multidimensional Signal Processing," *Proc. IEEE*, vol. 78, pp. 690-710, Apr. 1990.

[54] D. Marr, *Vision*, Freeman, San Francisco, 1982.

[55] G. Matheron, *Random Sets and Integral Geometry*, Wiley, New York, 1975.

[56] J. Mattioli, "Differential Relations of Morphological Operators," *Proc. Int'l Workshop on Math. Morphology and its Application to Signal Processing*, J. Serra and P. Salembier, Eds., Univ. Polit. Catalunya, Barcelona, Spain, May 1993.

[57] F. Meyer, "Integrals and Gradients of Images," *Proc. SPIE vol. 1769: Image Algebra and Morphological Image Processing III*, pp. 200-211, 1992.

[58] F. Meyer, "Topographic Distance and Watershed Lines," *Signal Processing*, vol. 38, pp. 113-125, July 1994.

[59] F. Meyer and S. Beucher, "Morphological Segmentation," *J. Visual Commun. Image Representation*, vol. 1, pp. 21–45, 1990.

[60] P.F.M. Nacken, "Chamfer Metrics, the Medial Axis and Mathematical Morphology," *J. Math. Imaging and Vision*, vol. 6, pp. 235–248, 1996.

[61] L. Najman and M. Schmitt, "Watershed of a Continuous Function," *Signal Processing*, vol. 38, pp. 99-112, July 1994.

[62] S. Osher and J. Sethian, "Fronts Propagating with Curvature-Dependent Speed: Algorithms Based on Hamilton-Jacobi Formulations," *J. Comput. Physics*, vol. 79, pp. 12–49, 1988.

[63] P. Perona and J. Malik, "Scale-Space and Edge Detection Using Anisotropic Diffusion," *IEEE Trans. Pattern Anal. Mach. Intellig.*, vol. 12, pp. 629–639, July 1990.

[64] Y. Pnueli and A. M. Bruckstein, "DigiDürer – A digital engraving system," *The Visual Computer*, vol. 10, pp. 277–292, 1994.

[65] F. Preteux, "On a Distance Function Approach for Gray-Level Mathematical Morphology," in *Mathematical Morphology in Image Processing*, E.R. Dougherty, Ed., Marcel Dekker, NY, 1993.

[66] R. T. Rockafellar, *Convex Analysis*, Princeton Univ. Press, Princeton, 1970.

[67] A. Rosenfeld and J. L. Pfaltz, "Sequential Operations in Digital Picture Processing," *J. ACM*, vol. 13, pp. 471-494, Oct. 1966.

[68] A. Rosenfeld and J.L. Pfaltz, "Distance Functions on Digital Pictures," *Pattern Recognition*, vol. 1, pp. 33–61, 1968.

[69] E. Rouy and A. Tourin, "A Viscocity Solutions Approach to Shape from Shading," *SIAM J. Numer. Anal.*, vol. 29 (3), pp. 867-884, June 1992.

[70] D. Rutovitz, "Data Structures for Operations on Digital Images," in *Pictorial Pattern Recognition*, (G.C. Cheng et al, Eds.), pp. 105–133, Thompson, Washington D.C., 1968.

[71] B.E.A. Saleh and M.C. Teich, *Fundamentals of Photonics*, Wiley, NY, 1991.

[72] P. Salembier and J. Serra, "Morphological Multiscale Image Segmentation," in *Visual Communications and Image Processing* (P. Maragos, Ed.), Proc. SPIE vol. 1818, pp. 620–631, 1992.

[73] G. Sapiro, R. Kimmel, D. Shaked, B. Kimia, and A. Bruckstein, "Implementing Continuous-scale Morphology via Curve Evolution," *Pattern Recognition*, vol. 26, pp. 1363–1372, 1993.

[74] G. Sapiro and A. Tannenbaum, "Affine Invariant Scale-Space," *Int'l J. Comp. Vision*, vol. 11, pp. 25–44, 1993.

[75] M. Schröder, "The Eikonal Equation," *Math. Intelligencer*, vol. 1, pp. 36–37, 1983.

[76] J. Serra, *Image Analysis and Mathematical Morphology*, Acad. Press, NY, 1982.

[77] J. Serra, editor, *Image Analysis and Mathematical Morphology. Vol. 2*, Acad. Press, NY, 1988.

[78] J. A. Sethian, *Level Set Methods*, Cambridge Univ. Press, 1996.

[79] F. Y.-C. Shih and O. R. Mitchell, "Decomposition of Gray-scale Morphological Structuring Elements," *Pattern Recognition*, vol. 24, pp. 195-203, 1991.

[80] P. Soille, "Generalized Geodesy via Geodesic Time," *Pattern Recogn. Lett.*, vol. 15, pp. 1235–1240, 1994.

[81] S. R. Sternberg, "Language and Architecture for Parallel Image Processing," in *Pattern Recognition in Practice* (E.S. Gelsema and L.N. Kanal, Eds.), North Holland Publ., 1980.

[82] H. Tek and B. B. Kimia, "Curve Evolution, Wave Propagation, and Mathematical Morphology," in *Mathematical Morphology and Its Applications to Image and Signal Processing* (H. Heijmans and J. Roerdink, Eds.), Kluwer Acad. Publ., 1998, pp. 115–126.

[83] R. van den Boomgaard, *Mathematical Morphology: Extensions towards Computer Vision*, Ph.D. Thesis, Univ. of Amsterdam, The Netherlands, 1992.

[84] R. van den Boomgaard and A. Smeulders, "The Morphological Structure of Images: The Differential Equations of Morphological Scale-Space," *IEEE Trans. Pattern Anal. Mach. Intellig.*, vol. 16, pp. 1101-1113, Nov. 1994.

[85] P. Verbeek and B. Verwer, "Shading from shape, the eikonal equation solved by grey-weighted distance transform," *Pattern Recogn. Lett.*, vol. 11, pp. 618–690, 1990.

[86] B.J.H. Verwer, Distance Transforms: Metrics, Algorithms, and Applications," Ph.D. Thesis, Tech. Univ. of Delft, The Netherlands, 1991.

[87] L. Vincent, "Exact Euclidean Distance Function by Chain Propagations," in *Proc. Conf. on Comp. Vision and Pattern Recognition*, pp. 520–525, Hawaii, 1991.

[88] L. Vincent, "Morphological Algorithms," in *Mathematical Morphology in Image Processing*, E. R. Dougherty, Ed., Marcel Dekker, NY, 1993.

[89] L. Vincent and P. Soille, "Watershed In Digital Spaces: An Efficient Algorithm Based On Immersion Simulations," *IEEE Trans. Pattern Anal. Mach. Intellig.*, vol. 13, pp. 583–598, June 1991.

[90] A. P. Witkin, "Scale-Space Filtering," *Proc. Int'l Joint Conf. Artif. Intellig.*, Karlsruhe, Germany, 1983.